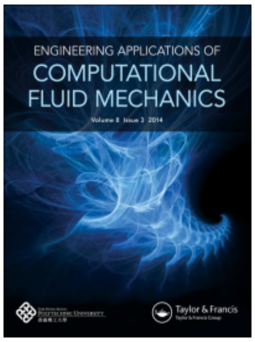

Taylor & Francis
Taylor & Francis Group

Engineering Applications of Computational Fluid Mechanics

ISSN: (Print) (Online) Journal homepage: https://www.tandfonline.com/loi/tcfm20

Computational study of free surface film flow and subsequent disintegration of a sheet and ligaments into droplets from a rotary disk atomizer

Kuldeep Singh, Stephen Ambrose, Richard Jefferson-Loveday, Andrew Nicoli & Sandeep Mouvanal

ENGINEERING APPLICATIONS OF COMPUTATIONAL FLUID MECHANICS
2023, VOL. 17, NO. 1, 2162971
https://doi.org/10.1080/19942060.2022.2162971

Taylor & Francis
Taylor & Francis Group

Computational study of free surface film flow and subsequent disintegration of a sheet and ligaments into droplets from a rotary disk atomizer

Kuldeep Singh, Stephen Ambrose, Richard Jefferson-Loveday, Andrew Nicoli and Sandeep Mouvanal

University Technology Centre in Gas Turbine Transmission Systems, Faculty of Engineering, The University of Nottingham, Nottingham, UK

ABSTRACT
In the present study, a computational methodology based on computational fluid dynamics (CFD) is developed to investigate free surface film flow and its subsequent disintegration on a rotary disk atomizer. The present study provides an insight into efficiently modeling both liquid film formation and its subsequent disintegration. The presented computational methodology can easily be reproduced and can act as a benchmark for the modeling of liquid film formation as well as the disintegration phenomenon. The influence of disk speed, liquid flow and feed arrangement on the rotating disk are investigated. The film thickness profile on the disk resembles the formation of spiral waves at 500 RPM and an irregular breakup of the spiral waves for a disk speed of 1000 RPM. At higher speeds, a smooth and thin liquid film is observed on the disk. Offset feeding of the liquid on the disk alters the wave formation and breakup of the spiral waves. It is found that ligaments are formed at the lip of the disk owing to Rayleigh–Taylor instability, whereas liquid sheet breakup is due to combined rim and wave disintegration for the parameters investigated in this study.

ARTICLE HISTORY
Received 15 September 2022
Accepted 21 December 2022

KEYWORDS
Rotating disk; atomizer; ligaments; CFD; VOF; multi-phase flow

Nomenclature

d	Diameter (m)
H	Height (m)
L	Length (m)
$\dot{m}$	Mass flow rate (kg/s)
N	Disk speed (RPM)
Oh	Ohnesorge number $(= \mu/\sqrt{\rho\sigma r})$
Q	Flow rate (m^3/s)
r	Radius (m)
Re	Reynolds number $(= 4\rho Q/\pi\mu r)$
t_d	Disk thickness (m)
t	Local time (s)
T	Disk revolution time (s)
u	Velocity (m/s)
Vr-mean	Mean radial velocity
w	Width (m)
We	Weber number $(= \rho u^2 r/\sigma)$

Acronyms

CD	Computational Domain
CFD	Computational Fluid Dynamics
CSF	Continuum Surface Force
LPM	Liters Per Minute
PLIC	Piecewise Line Interface Calculation
RANS	Reynolds Averaged Navier–Stokes
RT	Rayleigh–Taylor
SMD	Sauter Mean Diameter
SST	Shear Stress Transport
TD	Turbulence Damping
VOF	Volume Of Fluid

Greek

α	Volume fraction
ρ	Density (kg/m^3)
σ	surface tension (N/m)
θ	Angle (°)
Ω	Rotational speed (RPM)
μ	Viscosity (Pa·s)
ω	Angular velocity (rad/s)

1. Introduction

Rotary disk atomizers are disintegrating systems where feed liquid is distributed centrally onto a disk and centrifugally accelerated to a high velocity. This liquid is eventually discharged as droplets into the surrounding air/gas atmosphere. The film formation mechanism on a rotary disk atomizer and the subsequent disintegration into ligaments and droplets is depicted in Figure 1. These atomizers are widely utilized in the pharmaceutical

CONTACT Kuldeep Singh Singh@nottingham.ac.uk

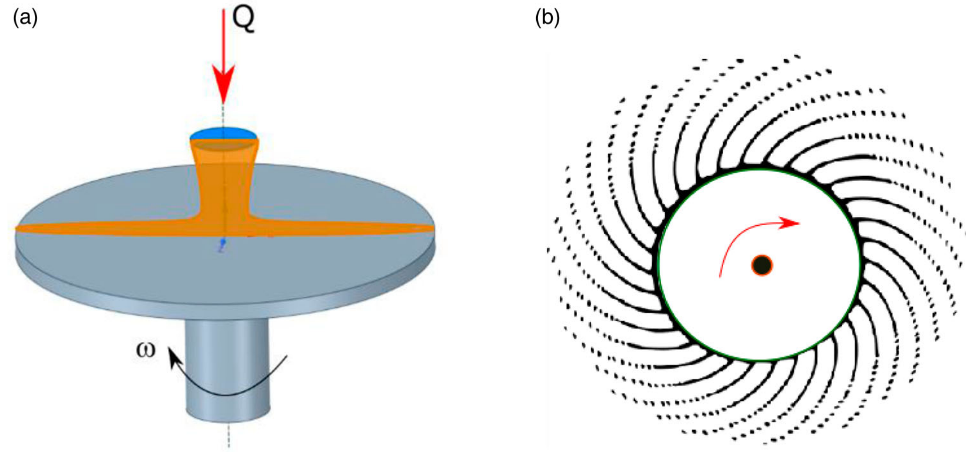

Figure 1. (a) Film formation; (b) ligament and drop formation on rotary disk.

industries for oral and injectable encapsulation (Kheyfets & Kieweg, 2013), in the food industries for nutritional stability and taste masking (Gibbs Inteaz Alli et al., 1999), in the metallurgical industries for waste heat recovery and granulation (Wu et al., 2015), in the agricultural industries for animal feeds, for spreading pesticides in fields and in the food-processing industries (Frost, 1981).

Liquid film formation on rotating disks has been studied experimentally, theoretically and numerically. Turkyilmazoglu (2019, 2022) investigated rotating disk numerically. Charwat et al. (1972) studied the flow and stability of thin liquid films on a rotating disk experimentally. They reported: (i) the formation of steady film flow; (ii) formation of concentric waves near the center; (iii) the formation of spiral waves; and (iv) the breakup of spiral waves on a rotating disk. However, the occurrence of these waves was dependent on disk speed, flow rate and fluid properties. The experimental study of Woods (1995) reconfirmed the presence of concentric and spiral waves. Moreover, this study highlighted that the small amplitude wave assumptions in the theoretical models were not appropriate, as large amplitude waves were generated on the rotating disk.

Rice et al. (2005) carried out computational fluid dynamics (CFD) analysis on the free surface film from a liquid jet impinging over a rotating disk. A two-dimensional axisymmetric model was used to predict film formation and film evaporation. Mantripragada and Sarkar (2017) performed a steady-state two-phase turbulent CFD study to determine the liquid film thickness on a spinning disk. They demonstrated that the liquid film thickness at the edge increases with increasing Reynolds (Re) and Ohnesorge (Oh) numbers. This study only focused on the surface film, and as such, disintegration of the film was not investigated. However, a correlation was proposed to relate the film thickness to the droplet diameter. Recently, Nicoli et al. (2022) investigated lubricating-oil film formation on the rotating cup using high fidelity VOF and a computationally efficient Eulerian thin film model (ETFM) for aeroengine applications. They reported that the predictions of the ETFM model were comparable with high fidelity VOF at lower computational cost.

Numerous experimental studies are available in the open literature describing the breakup mechanisms of liquid from rotating disks or cups. One of the earlier studies on rotating cups, by Hinze and Milborn (1950), identified three different breakup mechanisms and classified them as: direct drop, ligament and sheet. Frost (1981) studied liquid disintegration from a spinning disk experimentally. A flow map indicating direct droplet, ligament and a mixture of ligament and sheet regimes was produced based on dimensional analysis. This study provided transition criteria from one mode of disintegration to another mode based on a critical liquid flow rate and the operating speed of the disk. This study also proposed correlations for estimating the number of ligaments and droplet formation frequency. Glahn et al. (2002) and J. Liu et al. (2012) also proposed correlations to map the transitions from the direct droplet, ligament and sheet regimes. These correlations are summarized in Table 1. Cageao et al. (2022) investigated oil shedding from a rotating cup geometry experimentally. In this study, a shaft passed through the rotating cup geometry, which is typically found in aeroengine bearing chambers. For this geometric configuration, they provided a flow map highlighting the transitions between droplets-ligaments and ligaments-sheet regime.

Wang et al. (2015) investigated disintegration mechanisms in the ligament regime from a spinning disk using CFD for heat recovery in the metallurgical industries. They performed a three-dimensional transient sector

Table 1. The correlations proposed by Frost (1981), Glahn et al. (2002) and J. Liu et al. (2012) to identify the transition from a direct droplet to ligaments and from ligaments to a sheet.

	Droplet to ligaments transition /Full ligaments	Ligament to sheet transition /First appearance of sheet
Frost (1981)	$\left(\frac{Q\rho}{\mu D}\right)\left(\frac{\omega\rho D^2}{\mu}\right)^{0.63} > 0.46\left(\frac{\sigma\rho D}{\mu^2}\right)^{0.9}$	$\left(\frac{Q\rho}{\mu D}\right)\left(\frac{\omega\rho D^2}{\mu}\right)^{0.84} < 19.8\left(\frac{\sigma\rho D}{\mu^2}\right)^{0.9}$
Glahn et al. (2002)	$V^+ = 0.0854\ \mathrm{Oh}^{-0.9}\mathrm{We}*^{-0.85}$	$V^+ = 0.1378\ \mathrm{Oh}^{-0.33}\mathrm{We}*^{-0.435}$
J. Liu et al. (2012)	$Q > 6.5r^3\omega\left[\frac{\rho\omega^2 r^3}{\sigma}\right]^{-1.161}\left[\frac{\mu^2}{\rho\sigma r}\right]^{-0.0705}$	$Q > 5.13r^3\omega\left[\frac{\rho\omega^2 r^3}{\sigma}\right]^{-0.789}\left[\frac{\mu^2}{\rho\sigma r}\right]^{0.036}$

analysis using a VOF approach with the k–ϵ turbulence model. Additionally, the size of the periodic sector was not stated but was selected in such a way that at least two ligaments were captured within the selected size of the periodic sector. The spacing between ligaments was dependent on the geometric and operating conditions. Hence, the size description of the sector provided by Wang et al. (2015) makes the simulation process trivial. Moreover, the film thickness and velocity inputs for the computational domain were taken from the earlier numerical work of Wang et al. (2014), which was represented by complex equations and is not easy to reproduce.

The present study is carried out using CFD, as CFD-based studies are widely used for industrial applications such as those presented by Lee et al. (2021), G. Liu et al. (2021) and Yuan et al. (2021).

The main endeavor of the present study is as follows.

- The majority of the theoretical and CFD studies in the literature ignore wave formation on the disk and focus only on the radial distribution of the film thickness. These waves are expected to have a strong influence on the heat and mass transfer. In the present study, the formation of free surface waves, and the breakup of surface waves and their influence on the liquid film thickness and film velocity are discussed for disk speeds in the range 500 to 2500 RPM and liquid flow rates in the range 0.3 to 2.4 LPM. A qualitative comparison of free surface waves and experimental studies is discussed.
- In most experimental and numerical studies, liquid is fed in at the center of the rotating disk. These studies are relevant to the pharmaceutical industries. However, liquid film formation onto the rotating elements from the offset feed is common in aeroengines. Hence, in this study film formation on a rotating disk using both center feed as well as offset feed has been investigated.
- The studies available in the open literature are either focused on free surface film flow or disintegration mechanisms. The computational requirements to capture film formation on the disk is significantly lower than that required to capture liquid film disintegration. In the literature, boundary conditions imposed on the computational domain used to model liquid film disintegration is taken from complicated analytical relations. It is hard to reproduce the results presented in the literature following the described methodology. The present study provides an insight to model efficiently both liquid film formation and its subsequent disintegration. The presented computational methodology can easily be reproduced and can act as a benchmark for modeling liquid film formation as well as the disintegration phenomenon. A detailed discussion of the grid resolution required for modeling thin film formation and disintegration is also added for ease of reproducing results or utilizing the methodology presented.

2. Problem description and computational domain

In the present study, liquid film formation on a rotating disk and its subsequent disintegration into sheets and ligaments is analyzed using CFD. The investigated configuration consists of a disk rotating along the centerline with liquid fed from either above the centerline or offset from the centerline position. Figure 2 depicts the disk and liquid feed arrangement. The dimensions of the disk and liquid feed pipe are adopted from the experimental study of Wang et al. (2016). The investigated disk diameter (d) is 50 mm, the spacing between the disk and the liquid feed pipe (H) is 5 mm and the diameter of the feed pipe (d_{pipe}) is 8 mm.

The grid resolutions required to capture a continuous film and disintegration of liquid at the rim of the disk are different. Hence, the whole process is modeled using two computational domains. Figures 2(c) and 2(d) depict these computational domains (CDs). The first computational domain (CD1) is used to predict film thickness on the disk and is modeled as a full 360° model. The height of this computational domain is equivalent to the spacing between the disk and the liquid feed pipe (H). The second computational domain (CD2) is used to predict the disintegration mechanism from the rim of the disk. Wang et al. (2015) recommended that the size of the periodic sector should be sufficient to accommodate two ligaments. In the present study, a 45° sector of the disk is modeled

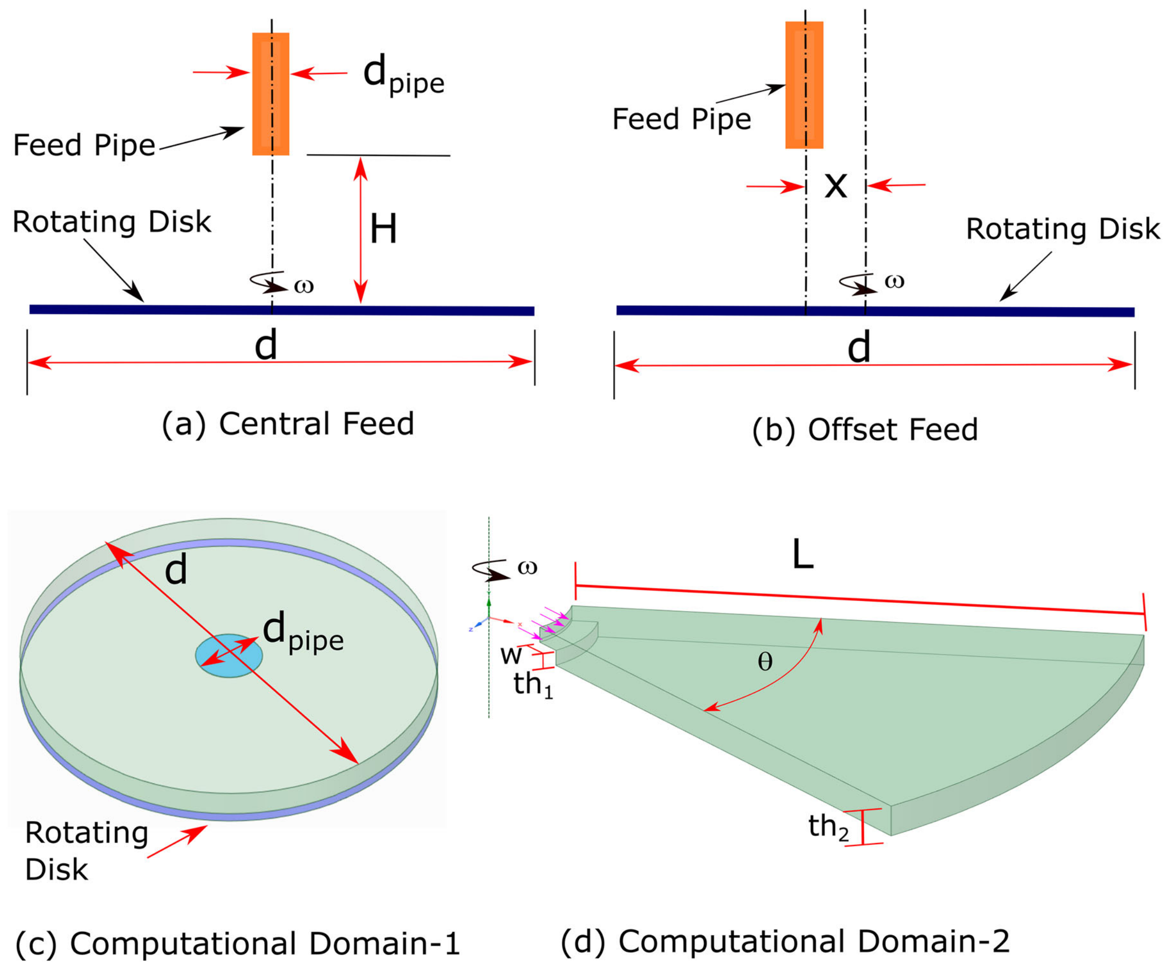

Figure 2. Liquid feed arrangement: (a) central feed; (b) offset feed; (c) computational domain used to predict film thickness over the disk; and (d) computational domain used to predict disintegration behavior. Artwork is prepared by the authors of this paper. Dimensions are available in the cited paper of Wang et al. (2016).

to capture the disintegration behavior. It is ensured that more than five ligaments are captured within the periodic sector to satisfy the periodic boundary conditions recommended by Wang et al. (2015). The length (L) of this computational domain is kept at $4d$ and the height of the computational domain (th_2) is twice the thickness of the disk ($\mathrm{th}_1 = 2.5$ mm). The rotating part of the disk, i.e. the rim width (w) in the second computational domain, is equal to the thickness of the disk (th_1). The film thickness on the disk and the film velocity components at various rotational speeds are extracted from CD1. These inputs are used to specify the boundary conditions of the film inlet in CD2.

2.1. Numerical methodology

In order to capture ligament/sheet formation and disintegration into droplets from a rotating disk, accurate capturing of a dynamic and sharp air–liquid interface is required. The VOF methodology is used in combination with a piecewise linear interface calculation (PLIC) to track the air–liquid interface location following Wang et al. (2015).

2.1.1. Governing equations

In the present study, the flow is assumed to be incompressible. The phenomena under investigation are essentially three-dimensional and transient. The governing equations—continuity and momentum equations—are solved using the finite-volume-method-based solver ANSYS® Fluent® (ANSYS Inc. (US), 2020).

$$\nabla \cdot u = 0 \tag{1}$$

$$\rho \left[\frac{\partial u}{\partial t} + \nabla \cdot (uu) \right] = -\nabla p + \nabla \cdot (\mu \nabla u) + \rho g + F_{\mathrm{st}} \tag{2}$$

where u is the velocity vector, ρ is the density of liquid, p is the pressure, μ is the dynamic viscosity of liquid or gas, g is the gravitational acceleration, F_{st} is the surface tension term. The Euler–Euler multiphase method is used. The Euler–Euler approach with the VOF method is used to simulate the multiphase flow. In the VOF model, a single set of momentum equations is shared by both the phases (liquid and gas), and the volume fraction of each of the phases in each computational cell is tracked throughout the domain. The continuum surface force (CSF) method of Brackbill et al. (1992) is used to model the surface tension term.

$$F_{st} = \sigma\kappa \frac{\nabla\alpha}{\alpha_{max} - \alpha_{min}} \tag{3}$$

where σ is the surface tension, κ is the local curvature, α is the volume fraction, which acts as an indicator to locate the interface using the VOF method. At the interface, the value of the volume fraction is in the range $0 < \alpha < 1$ and obeys the transport equation, Equation (4):

$$\frac{\partial\alpha}{\partial t} + \nabla\cdot(\alpha u) = 0 \tag{4}$$

In the present study, flow is assumed to be turbulent. The boundary layer on a rotating disk experiences laminar to turbulent transition at Reynolds number ≈ 500, owing to the presence of primary and secondary global instabilities as reported by Imayama et al. (2013) and Appelquist et al. (2018). For the investigated parameters in this study, the Reynolds number is in the range 2,250 to 11,200 at the edge of the disk, calculated based on the properties of air. Moreover, the condition of the free surface liquid film flow can be determined based on the Reynolds number ($Re_S = Q/2\pi r\upsilon$) criterion proposed by Brauer (1958). A free surface film is turbulent for $Re_s > 20$. For the investigated flow rates in the present study, the liquid film is also turbulent towards the center of the disk. Bhatelia et al. (2009) investigated film formation on a rotating disk assuming laminar film flow. A significant deviation from the experimental results was reported in this study, whereas Pan et al. (2010) assumed a turbulent film and obtained good agreement with the experimental results for the identical geometric and operating conditions. Hence, the assumption of turbulent flow is valid.

In order to model turbulence, a Reynolds Averaged Navier–Stokes (RANS) approach is used to account for the effect of turbulence following ANSYS Inc. (US) (2020) and Sun et al. (2015). Because of the Reynolds averaging method, the Reynolds stresses ($-\rho\overline{u_i'u_j'}$) appear in the second term on the right-hand side of Equation (2). The Boussinesq hypothesis, given in Equation (5) is used to calculate the Reynolds stresses:

$$-\rho\overline{u_i'u_j'} = \mu_t\left(\frac{\partial u_i}{\partial x_j} + \frac{\partial u_j}{\partial x_i}\right) - \frac{2}{3}\rho k\delta_{ij} \tag{5}$$

where $\acute{u}$ is the fluctuating component of velocity, μ_t is turbulent viscosity and k is the turbulent kinetic energy per unit mass. The shear stress transport (SST) k–ω turbulence model is used to achieve closure of equations, based on the recommendations of Bristot et al. (2016). In order to model turbulent momentum transfer accurately at the interface of the liquid and gas phases in the VOF approach, the turbulence damping method proposed by Egorov (2004) is adopted in the present study. A source term in the ω equation of the k–ω model is implemented, given by Equation (6):

$$A \cdot \Delta y\beta\rho_i\left(B\cdot\frac{6\mu_i}{\beta\rho_i\Delta n^2}\right)^2 \tag{6}$$

where A is the interface area density, the subscript i represents the ith phase, β is the closure coefficient of the destruction term, ρ is the density, B is a scaling coefficient known as the turbulence damping factor, μ is the dynamic viscosity and Δn is the near-wall cell height. A turbulence damping factor of $B = 10$ is considered in the present study based on the recommendation of Egorov (2004).

2.1.2. Operating conditions and fluid properties

In the present study, aeroengine oil Eastman-2197 is used as the working fluid and ambient air is considered as the gaseous phase. The properties of the working fluid used in this study are given in Table 2. The liquid flow rate required to produce ligaments and sheets for a given disk speed is determined from the analysis of the correlations proposed by Frost (1981), Glahn et al. (2002) and J. Liu et al. (2012). These correlations are given in Table 1. A flow map chart is produced based on these correlations for the disk size and fluid properties investigated in the present study as depicted in Figure 3. The lines in this figure represent the transition from the droplets to the ligament regime or the ligament to the sheet regime. The liquid flow rate was selected in such a way that, for a specific disk speed, the liquid disintegrates within either the ligament regime or the sheet regime.

2.1.3. Boundary conditions

The boundary conditions imposed on the computational domains are depicted in Figure 4. The first computational domain, Figure 4(a), is used to predict the film thickness on the disk. The disk is specified as a rotational wall such that the circumferential velocity at the

Table 2. Fluid properties of air and Eastman-2197 (Cageao et al., 2022).

Properties	Air	Eastman-2197
Density (kg/m^3)	1.225	978
Viscosity (Pa·s)	$1.789{,}4 \times 10^{-5}$	0.0262
Oil–air surface tension (N/m)	0.030,74	

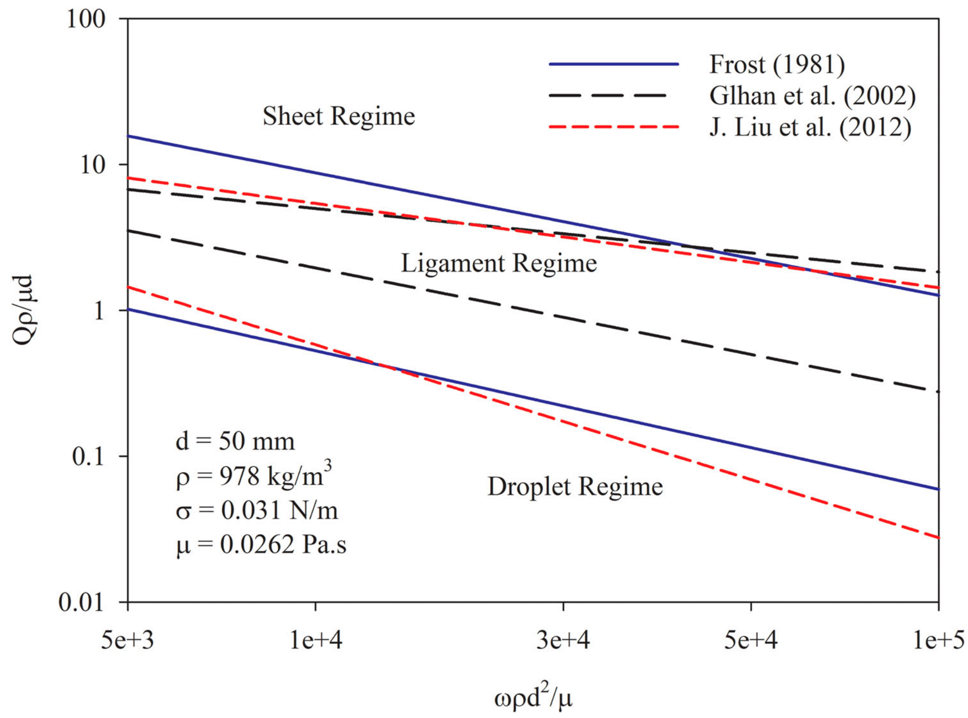

Figure 3. Flow map produced from the correlations of Frost (1981), Glahn et al. (2002) and J. Liu et al. (2012) for the investigated disk size and Eastman-2197 engine oil.

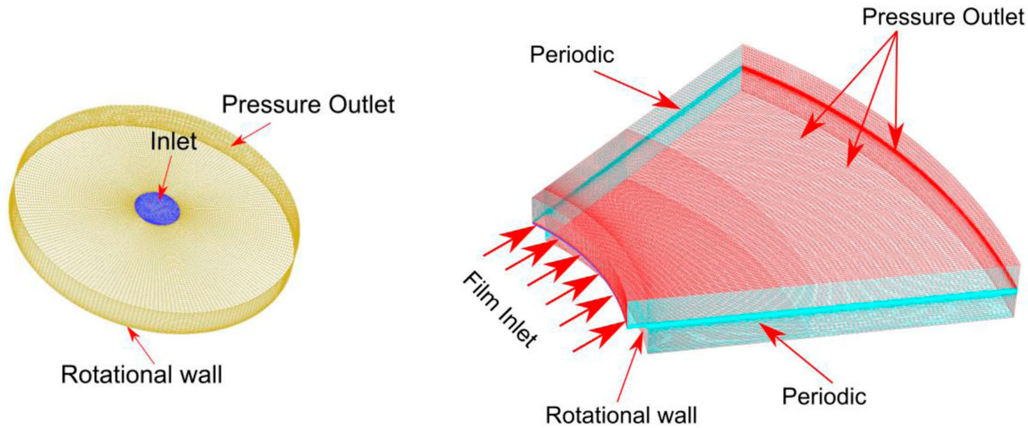

Figure 4. Typical mesh and boundary conditions for: (a) CD1; (b) CD2.

surface of the disk is $\omega \times r$. The disk speed is varied from 500 to 2500 RPM. The liquid mass flow rate ($\dot{m} = \rho Q$) is specified at the inlet such that the velocity component is $v = 4\dot{m}/(\rho\pi d^2)$. The volumetric flow rate considered in this study is in the range 0.3 to 2.4 LPM. The rest of the domain is specified as a pressure outlet. The second computational domain, Figure 4(b), is used to predict the disintegration mechanism from the rim of the disk. From the first computational domain, film thickness and film velocity components at various rotational speeds are extracted 2.5 mm away from the edge of the disk. The film thickness obtained from CD-1 is used to model the height of the input in CD-2 and the film velocity components are used to specify thhe boundary conditions in the second computational domain. A 45° sector of the disk is modeled to capture the disintegration behavior and the periodic boundary conditions are applied on both sides of the domain. The rotating disk is given rotational wall boundary conditions and the remaining faces in the computational domain are considered as pressure outlet boundaries.

2.1.4. Solution procedure

A coupled algorithm is used for pressure–velocity coupling; details of the schemes implemented can be found in the ANSYS Fluent theory guide (ANSYS Inc. (US), 2020). The second-order upwind scheme is used to

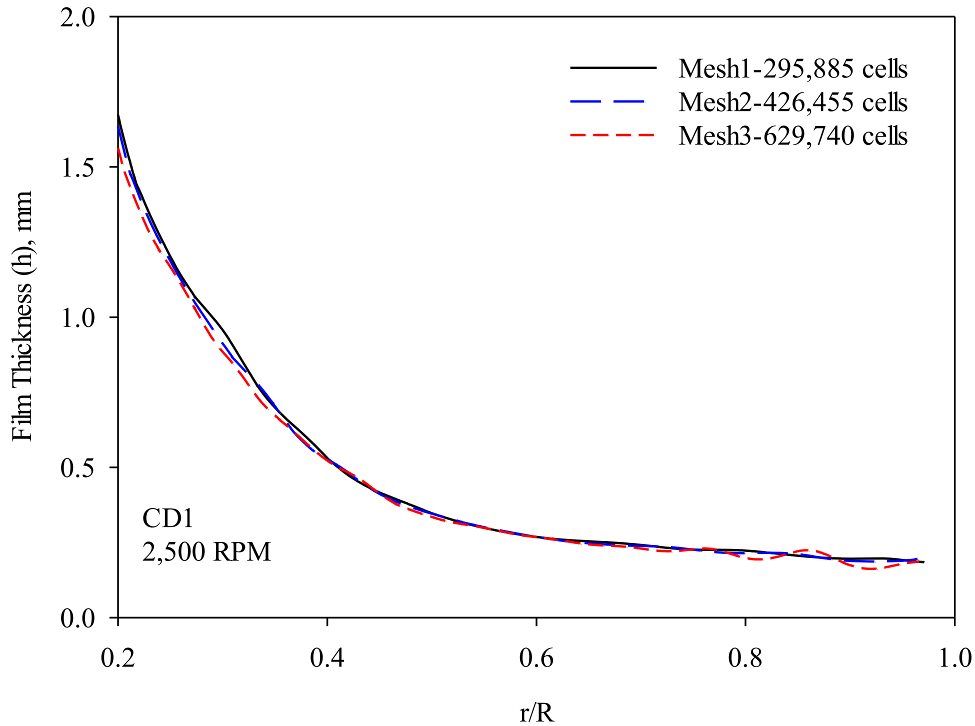

Figure 5. Radial distribution of mean film thickness for the investigated grids on computational domain 1 (CD1).

discretize of the convective terms. The absolute residual convergence criterion of 10^{-5} is used to determine convergence. For all the simulations, the maximum Courant–Friedrichs–Lewy (CFL) number is kept at 0.5 for numerical stability (ANSYS Inc. (US), 2020) and adaptive time steps are used to maintain the CFL number at 0.5. The maximum number of iterations per time step is kept to 30 in order to make sure that the absolute residual convergence criterion is met in each time step. All simulations are run on the high-performance computing (HPC) facility Augusta/G2TRC, in which each G2TRC compute node has 44 cores and 192 GB of memory, with Intel® Xeon® Gold 6138 20C 2.0 GHz processors. On average, 5000 CPU hours are used to simulate one test case of CD-1 and 80,000 CPU hours to simulate one test case of CD-2.

2.2. Grid sensitivity study

In the present study, non-uniform structured grids are used for both the computational domains. Grids are generated using ICEM, a pre-processor to ANSYS Fluent. A grid sensitivity study is conducted for both the computational domains. For the first computational domain (CD1), the grid size is varied from 295,855 cells to 629,740 cells. The first cell-center is located at 25, 20 and 15 μm normal to the disk surface for the grids investigated. The number of cells in the wall normal direction for the first 500 μm spacing are 6, 8 and 10, respectively, for the selected grids. The radial distribution of the film thickness for the investigated grids at 2500 RPM and 0.9 LPM is shown in Figure 5. Under these operating conditions, the thinnest film, and hence the most grid dependent solution, is expected. It can be observed that, across all cases, a low mesh-dependency for the radial distribution of the mean film thickness is achieved. A maximum difference of 0.9% in the film thickness between the coarse grid and the fine grid is observed. For the coarse grid, only three cells are available to resolve the minimum film thickness observed in this case. A higher grid resolution is required to capture wave formation. Hence, it is decided to select Mesh2 (426,455 cells), which contains five cells, to resolve the minimum film thickness for further studies using CD1.

The second computational domain is utilized to predict the liquid disintegration mechanism. The rotational speed of the disk investigated for this domain is kept at 1500 RPM. Liquid flow rates are varied from 0.9 LPM for the ligament regime to 2.4 LPM for the sheet regime. Capturing instabilities at the rim of the disk is important for this domain. It is expected that the growth of instabilities and breakup of the sheet into droplets will be quick and challenging for the sheet regime. Consequently, operating conditions for the sheet regime are selected for the grid sensitivity studies. Three grids of 2,039,352, 3,651,252 and 4,821,372 cells are investigated. The first cell centers normal to the disk are kept at 15, 10 and 7.5 μm and the numbers of cells in the first

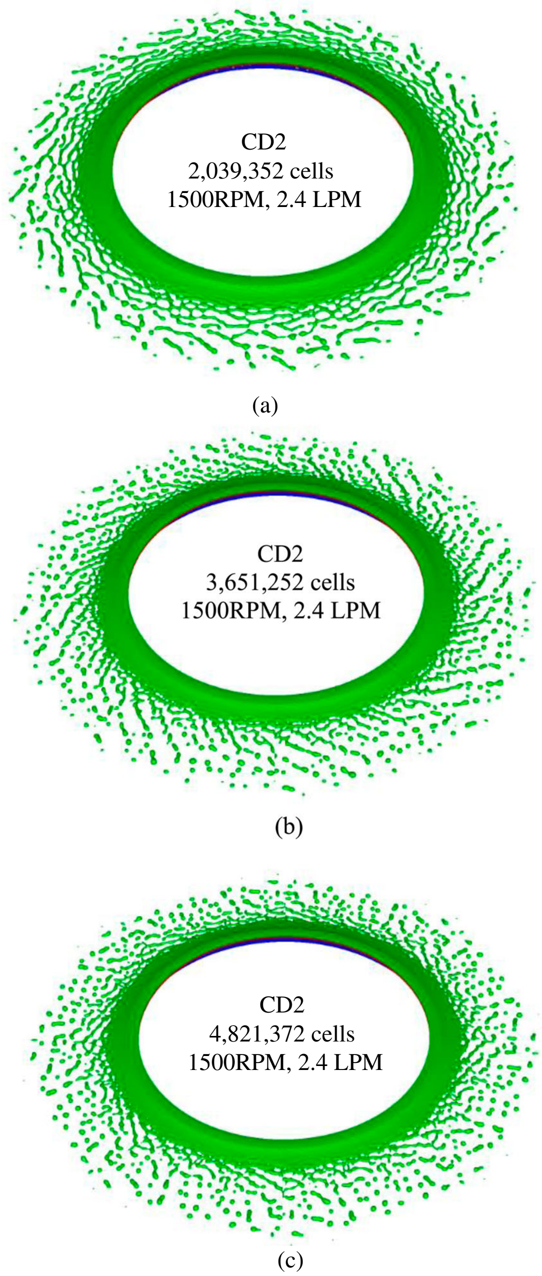

Figure 6. A qualitative comparison of sheet disintegration for the investigated grids on computational domain 2 (CD2).

500 μm in the wall's normal direction are 15, 20 and 25, respectively, for the investigated grids. The radial sheet-extents of the film for the grids investigated are 3.58, 3.71 and 3.715 mm, respectively. A qualitative comparison of the radial sheet extent and sheet disintegration into droplets is depicted in Figure 6. Quantitatively and qualitatively, the radial sheet extents and disintegration of the sheet for 3,651,252 and 4,821,372 cells are almost identical. A slight deviation in the sheet disintegration is observed for the mesh with 2,039,352 cells. Finally, the mesh with 3,651,252 cells is selected for further studies on CD2.

2.3. Validation of computational methodology

2.3.1. Free surface film flow on the rotating disk

The experimental study of Wang et al. (2020) is used to validate the present numerical model and numerical methodology that are used to model the free surface film flow, i.e. CD1. For the validation study, the disk size ($d = 100$ mm), fluid properties ($\rho = 1153$ kg/m^3, $\mu = 0.0108$ Pa·s, $\sigma = 0.067{,}64$ N/m) and operating conditions ($\Omega =$ 1500 RPM and $Q = 1.5$ LPM) are identical with the experimental conditions. The mean radial film velocity obtained from the present numerical model is compared with the experimental results in Figure 7. It can be observed that the present numerical results are in good agreement with the experimental measurements. This indicates that the present computational methodology is reliable and can be used to predict the free surface film flow characteristics over a rotating disk.

2.3.2. Ligament formation

The free surface film flow behavior is entirely different from that of the liquid film disintegration. A separate computational domain, i.e. CD2, is used for the predictions of liquid disintegration. Hence, an additional test case following the experimental study of Wang et al. (2016) is considered to validate the computational methodology used for film disintegration. For the validation study, the disk size ($d = 50$ mm), fluid properties ($\rho = 1170$ kg/m^3, $\mu = 0.0175$ Pa·s, $\sigma = 0.073$ N/m) and operating conditions (liquid feed rate $= 0.426$ LPM) are identical with the experimental conditions. Simulations are carried out for three disk speeds: 600, 1500 and 2100 RPM. The number of ligaments predicted at the investigated disk speeds from the present numerical model are compared with the experimental results in Figure 8. The model successfully predicts a ligament regime and the number of ligaments predicted at various disk speeds is found to be in good agreement with the experimental measurements. The predicted results are well within the uncertainty range of the experimental measurements. This suggests that the current modeling approach and mesh resolution are sufficient to investigate further the detailed flow physics of ligament formation and disintegration for this disk.

3. Results and discussion

3.1. Free surface film thickness on the rotating disk

3.1.1. Influence of rotational speed

The film thickness variation with the rotational speed of the disk is shown in Figure 9 in the radial and circumferential directions for a liquid feed rate of

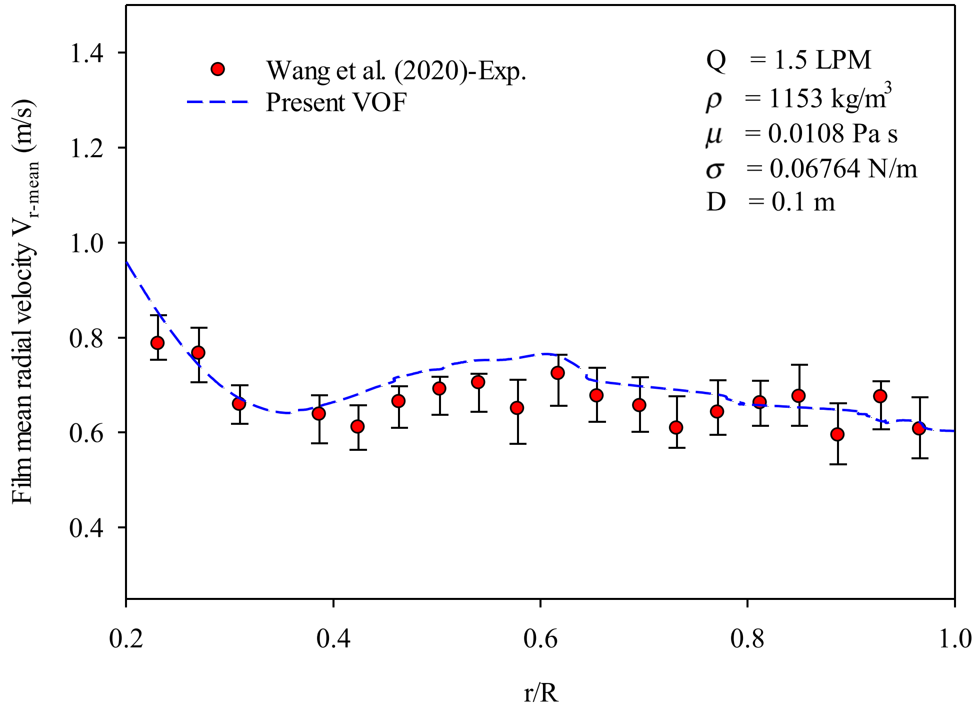

Figure 7. Comparison of mean film radial velocity with the experimental results of Wang et al. (2020).

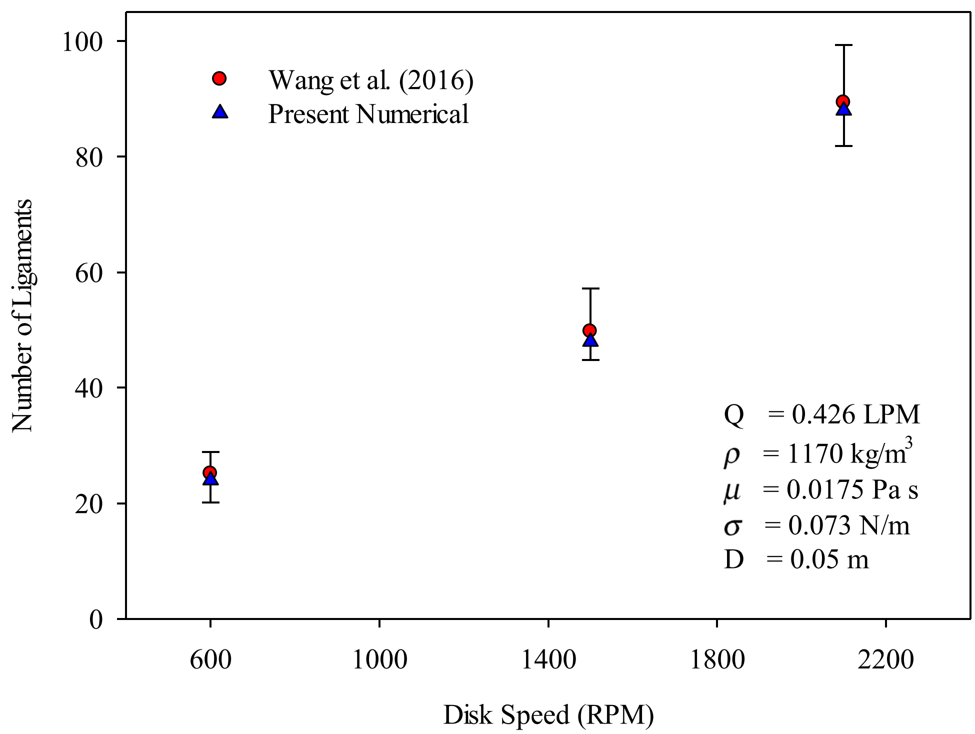

Figure 8. Comparison of number of ligaments with the experimental data of Wang et al. (2016).

0.9 LPM. It can be observed that, from Figure 9(a), the film thickness gradually decreases moving towards the edge of the disk. It is also evident that the film thickness decreases as the disk speed is increased. At the midspan of the disk, the average film thickness varies from 1.18 to 0.31 mm as the disk speed is varied from 500 to 2500 RPM, respectively. Film flow on a rotating disk is governed by Coriolis and centrifugal forces along with viscous drag. The magnitudes of the Coriolis and centrifugal forces are dependent on the film velocity. The film velocity magnitude increases with the disk speed and with increasing radial distance from the center.

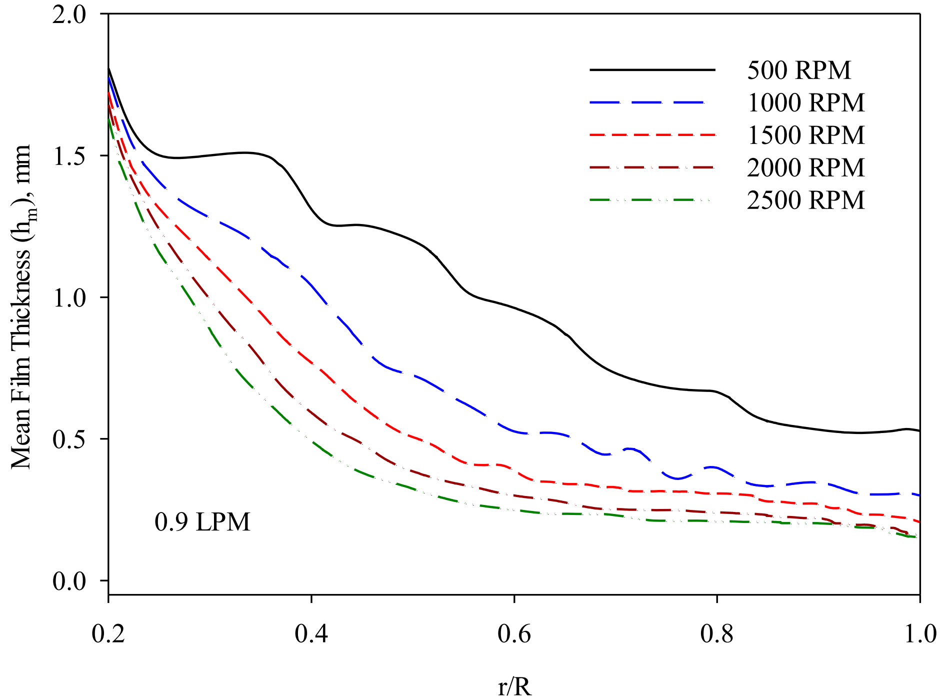

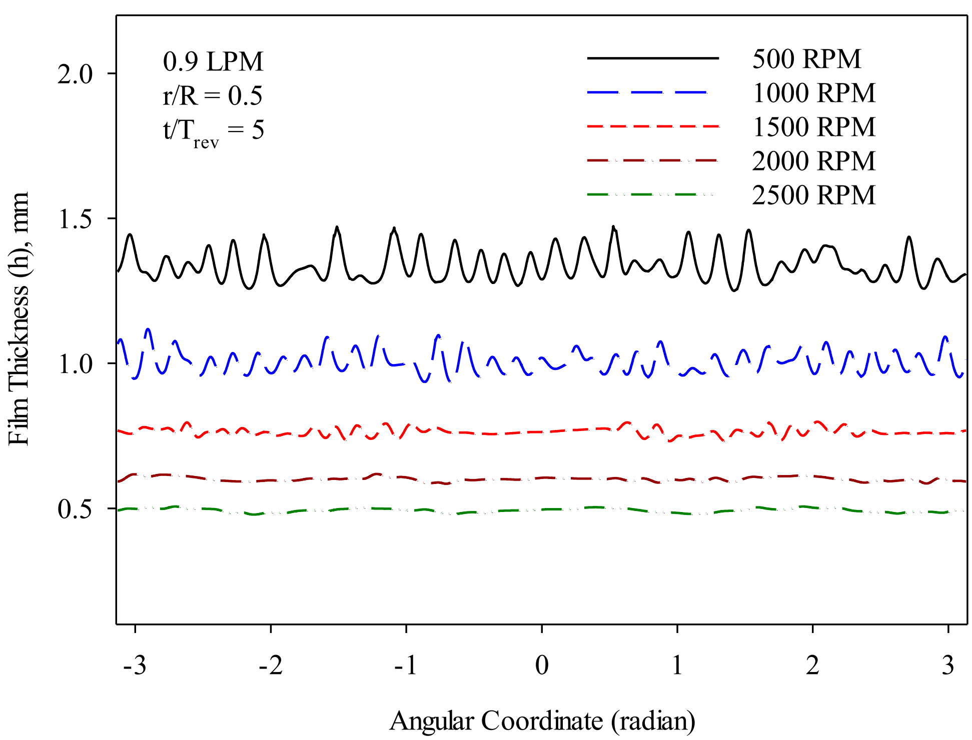

Figure 9. (a) Mean film thickness variation with disk speed along the radial direction; (b) instantaneous film thickness variation along the circumferential direction at $r/R = 0.5$, $t/T_{\mathrm{rev}} = 5$ and $Q = 0.9$ LPM.

Consequently, the magnitude of the Coriolis and centrifugal forces also increases. These forces are responsible for thinning of the film. The film velocity magnitude near the center of the disk is low, and hence the Coriolis and centrifugal forces are not dominating; inertia and viscous forces play an important role near the center of the disk. A thicker and wavy film is an outcome of these contradicting forces, especially at lower disk speeds.

The film thickness profile variation in the circumferential direction at $r/R = 0.5$ for $t/T_{\mathrm{rev}} = 5$ is shown in

Figure 9(b). A wavy film profile is observed for the disk speeds investigated. However, the amplitude of the waves decreases with an increase in disk speed. The maximum wave amplitudes at $r/R = 0.5$ and $t/T_{\mathrm{rev}} = 5$ are 130, 107, 32, 18 and 14 μm for disk speeds of 500, 1000, 1500, 2000 and 2500 RPM, respectively. The contours of film thickness on the disk surface for the disk speeds investigated are shown in Figure 10. Film thickness is represented by iso-surfaces of constant volume fraction ($\alpha = 0.5$) of oil. The disk normal direction (y) has been scaled by two for better visibility of the film profile. A strong influence of disk speed on liquid film formation is evident from Figure 10. At a disk speed of 500 RPM, spiral waves are generated. These waves are characterized by sharp peaks and shallow troughs. The irregular breakup of spiral waves can be seen at a disk speed of 1000 RPM. The amplitude of these waves decreases with an increase in the disk speed and towards the edge of the disk. Experimental studies such as those of Espig and Hoyle (1965) and Charwat et al. (1972) reported the occurrence of these waves on a rotating disk. The occurrence of these waves depends on the liquid flow rate, rotation speed and thermophysical properties of the liquid (Charwat et al., 1972). Most of the analytical and numerical studies (Lepehin & Riabchuk, 1975; Mantripragada & Sarkar, 2017; Rauscher et al., 1973; Rice et al., 2005; Wang et al., 2014) ignored these waves. However, the occurrence of these waves is expected to alter heat transfer and species transport characteristics, and these should be captured depending on the criticality of the application.

3.1.2. Influence of liquid feed rate

The film thickness variation for the liquid feed rates investigated is shown in Figure 11 in the radial and the circumferential directions for a disk speed of 1500 RPM. The liquid feed rate has a significant influence on the film thickness, as shown in Figure 11. The film thickness increases with increasing liquid feed rate. At the midspan of the disk, the average film thickness is 0.326 mm for 0.3 LPM, 0.764 mm for 0.9 LPM and 1.09 mm for 2.4 LPM. For a given speed, the centrifugal and Coriolis forces remain the same, but an increase in liquid flow rate results in increased inertial and viscous forces. Increased viscous forces are responsible for increasing film thickness. It can also be noticed that film thickness continuously decreases with increasing radial position. A slight fluctuation in the film thickness profile is due to the presence of waves, as can be seen in Figure 12. Irregular breakup of spiral waves is noticed at 0.3 LPM, whereas regular spiral waves are noticed at 0.9 LPM. A further increment in the flow rate to 2.4 LPM results in damping of these waves owing to the increased viscous effects. The maximum wave amplitudes at $r/R = 0.5$ and $t/T_{\mathrm{rev}} = 5$ are 38, 32 and 17 μm for liquid feed rates of 0.3, 0.9 and 2.4 LPM, respectively. A thinner liquid film in aeroengine applications can promote heat transfer owing to evaporation, but at the same time scarcity of lubricating oil and dry patches can increase risk to the structural integrity of the components. This can also lead to degradation of the lubricating oil. On the other hand, higher flow rates demand more pumping power. Hence, an optimum feed rate is desired.

3.1.3. Influence of offset feeding

Film thickness variations for the central and offset feed arrangements are shown in Figure 13 in the radial and circumferential directions for a disk speed of 1500 RPM and a liquid feed rate of 0.9 LPM. The radial variation of film thickness is plotted at a circumferential location of $3\pi/2$, as marked in Figure 13(a). At this location, the film thickness decreases with the increasing offset distance. This is because of the skewed film thickness for the offset feed arrangements as depicted in Figure 13(b). For the central feed arrangement, the mean film thickness is almost uniformly distributed in the circumferential direction. The occurrence of waves is entirely different for the offset feed arrangements as shown in Figure 14. The formation of spiral waves that unwind in the direction of rotation is observed in the case of the central feed arrangement. These waves cover the entire disk, but in the case of the offset feed arrangements, waves occur only on a segment of the disk ($0 \leq \theta \leq \pi$). The magnitude of the tangential velocity of the rotating disk is low at the location of the liquid feed for the central feed arrangement, and it is the same throughout the periphery of the impinging jet when it touches the rotating disk. On the contrary, the disk tangential speed is significantly higher at the point of liquid impingement for the offset feed arrangement. Since the tangential speed is proportional to the radial distance, hence the impinging liquid encounters a velocity difference throughout the periphery. This velocity difference keeps on increasing with the offset distance. This results in a non-uniform liquid film distribution over the surface of the rotating disk, as can clearly be observed in Figures 13 and 14. Film coverage and wave formation on the disk is expected to have a strong influence on the transport of heat and mass. The analytical correlations available in the open literature for a centrally fed disk cannot be used directly for an offset feed disk. Thus, the mean film thickness estimated from the analytical correlations may mislead designers. It is not always possible to feed lubricating oil centrally for aeroengine applications owing to design constraints. This may lead to non-uniform heat distribution and, as a consequence, thermal stress may increase. Hence, alternative

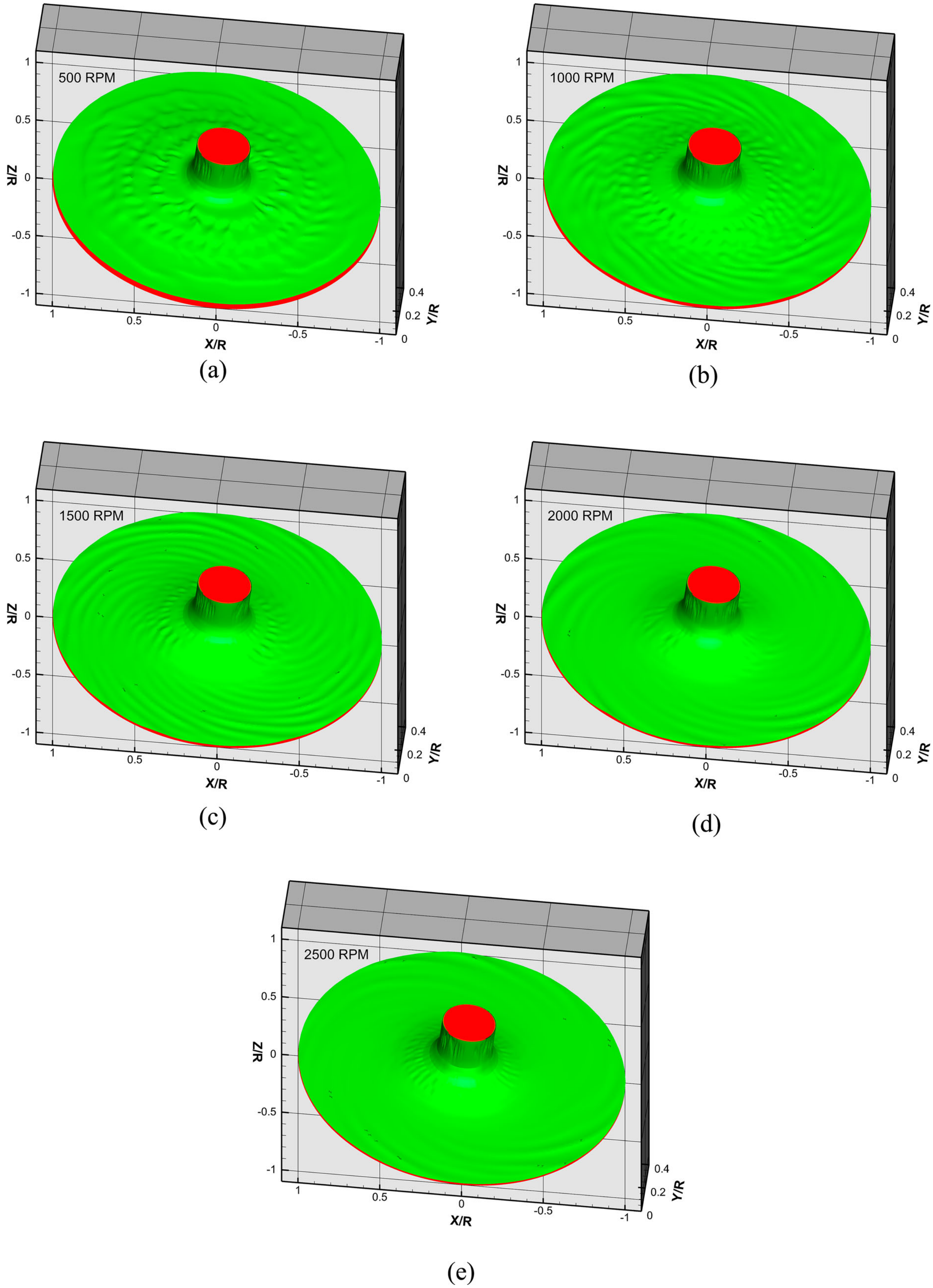

Figure 10. Instantaneous iso-surface of volume fraction 0.5 at $t/T_{\text{rev}} = 5$ for the disk speeds investigated.

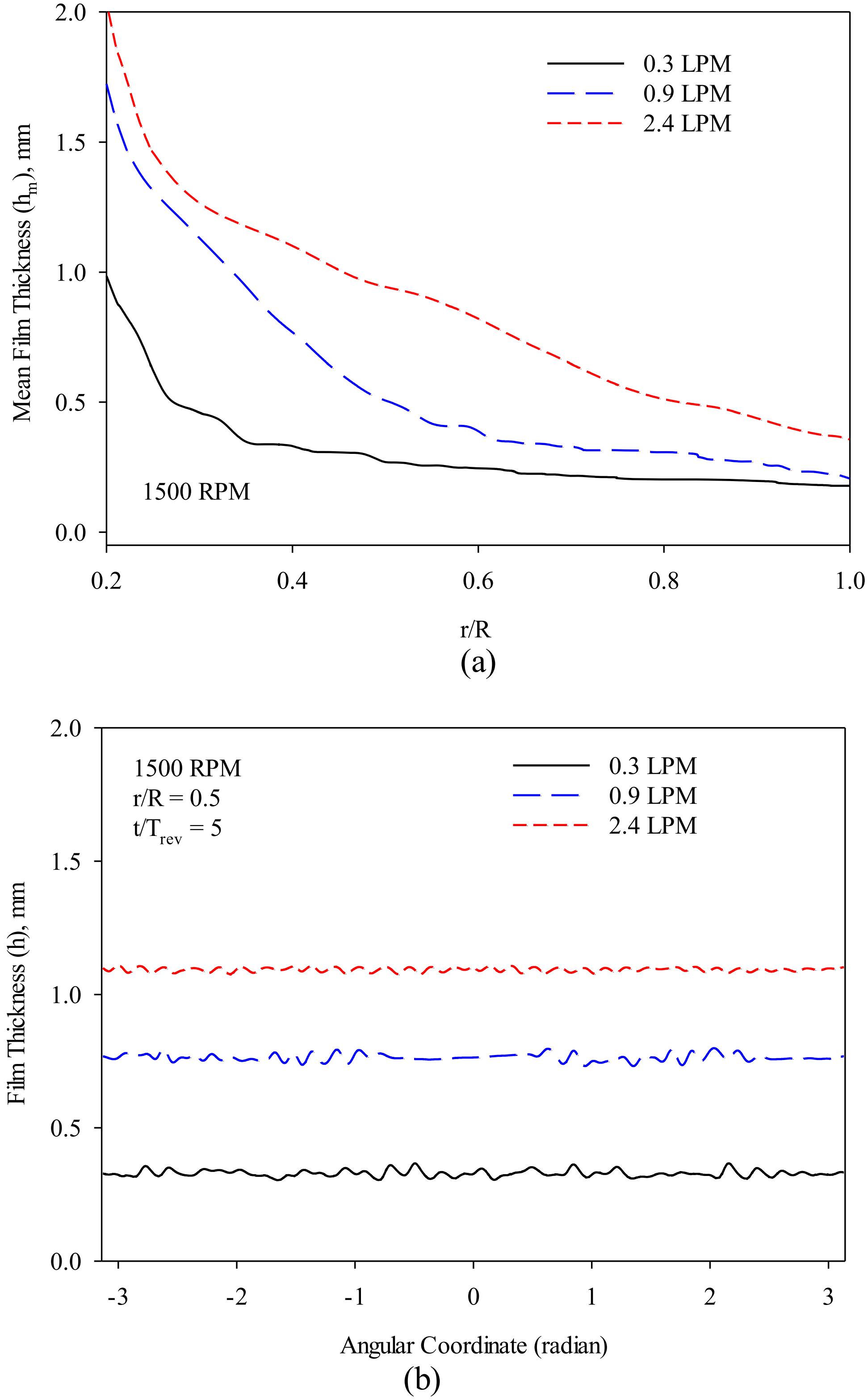

Figure 11. (a) Mean film thickness variation with liquid feed rate along the radial direction; (b) instantaneous film thickness variation along the circumferential direction at $r/R = 0.5$, $t/T_{\mathrm{rev}} = 5$ and $\Omega = 1500$ RPM.

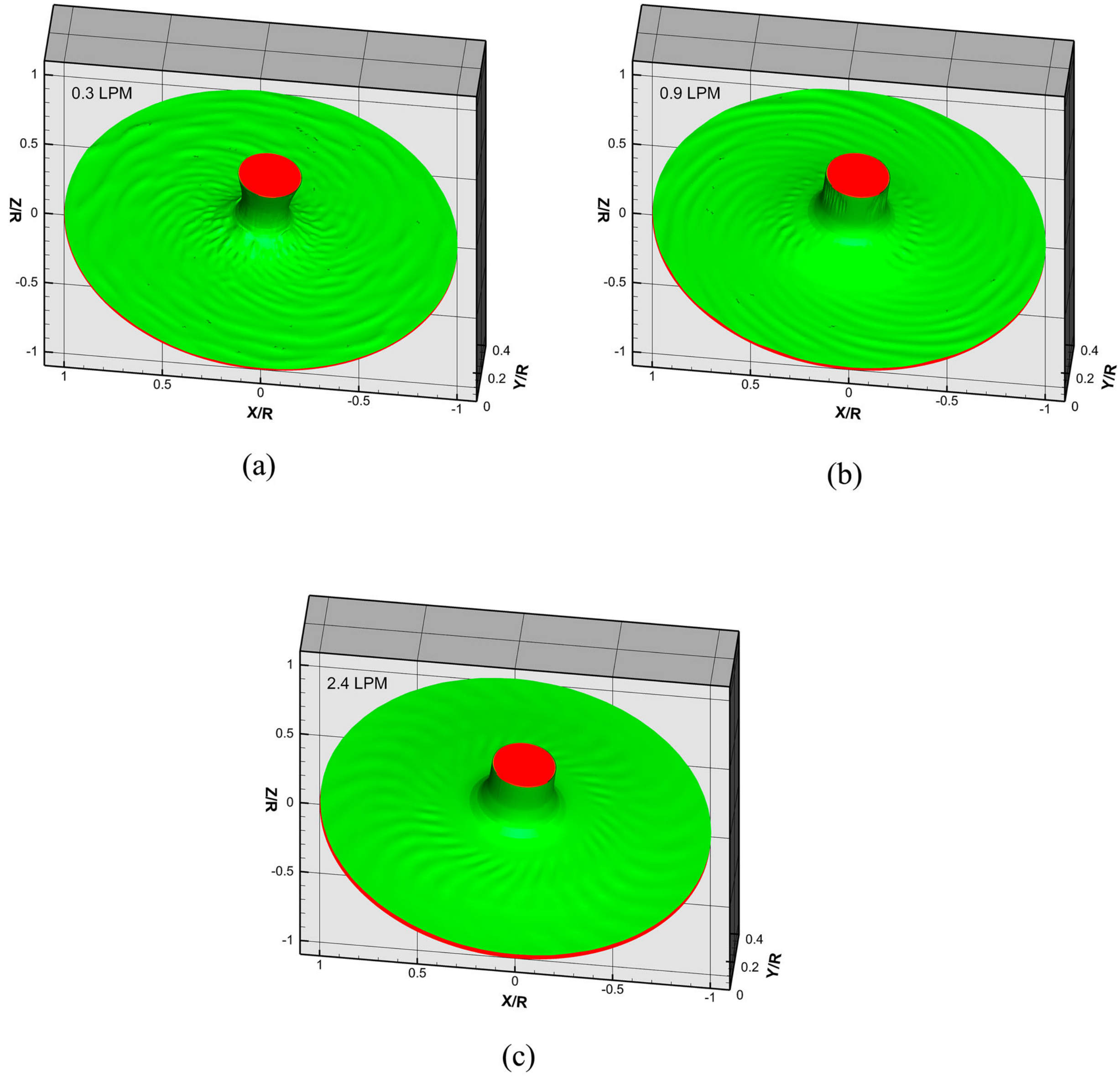

Figure 12. Instantaneous iso-surface of volume fraction 0.5 at $t/T_{\mathrm{rev}} = 5$ for the liquid feed rates investigated.

feed arrangements such as multiple feeding locations should be investigated to overcome these difficulties.

3.2. Free surface film velocity on the rotating disk

3.2.1. Influence of rotational speed

The variation of non-dimensional mean tangential and radial velocity with disk speed is shown in Figure 15 for the central feed arrangement at 0.9 LPM. The mean tangential and radial velocities are defined by Equations (7) and (8). These velocities are non-dimensionalized by the tangential velocity at the edge of the disk. The deviation of the mean tangential film velocity from the disk tangential velocity is known as the tangential slippage, which is an important parameter that governs the behavior of liquid film disintegration (Bizjan et al., 2014). A higher value of tangential slippage indicates excessive reduction in the film velocity. Reduction in the film velocity reduces centrifugal force, which is one of the main contributor forces for inducing instabilities in the liquid film and subsequent disintegration. A lower value of tangential slippage indicates better atomization efficiency.

$$V_{t-\mathrm{mean}} = \frac{1}{2\pi \times h(r,\theta)} \int_0^h V_t \mathrm{d}\theta \tag{7}$$

$$V_{r-\mathrm{mean}} = \frac{1}{2\pi \times h(r,\theta)} \int_0^h V_r \mathrm{d}\theta \tag{8}$$

It can be observed from Figure 15(a) that the non-dimensional mean tangential velocity increases with an increase in the disk speed. At the edge of the disk,

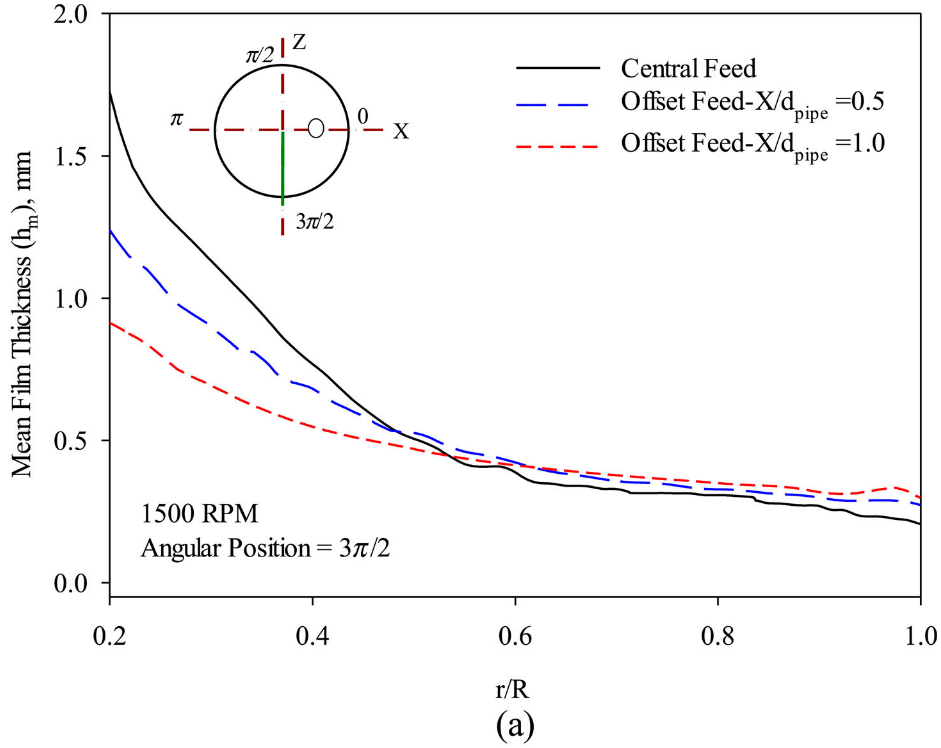

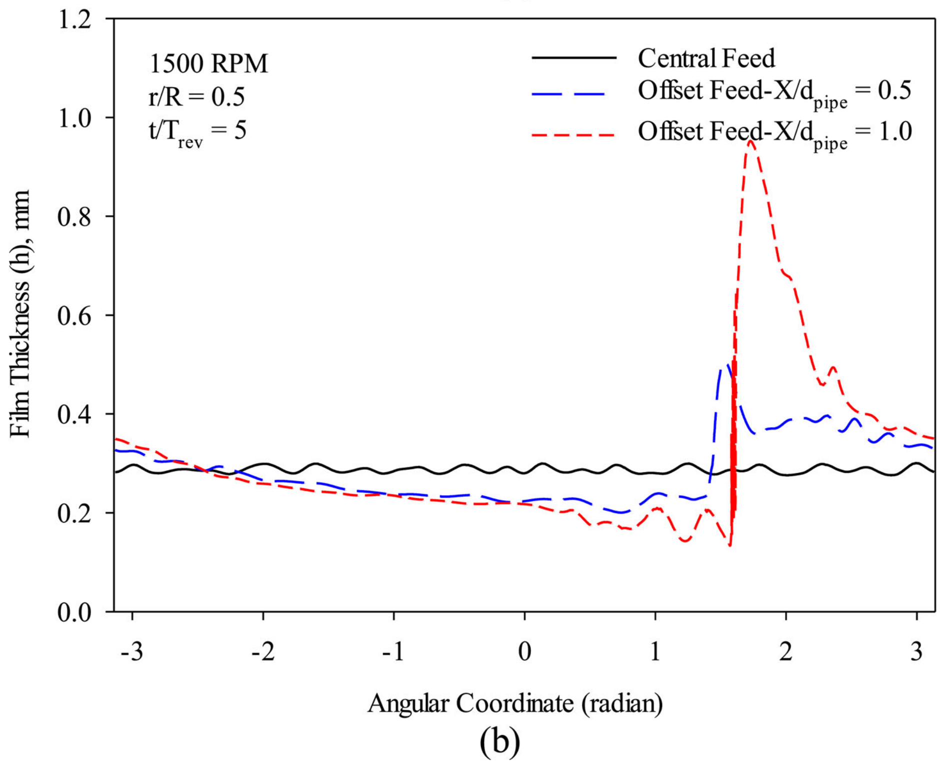

Figure 13. (a) Mean film thickness variation with liquid feed arrangement along the radial direction; (b) instantaneous film thickness variation along the circumferential direction at $r/R = 0.5$, $t/T_{rev} = 5$ and $\Omega = 1500$ RPM.

the non-dimensional mean film velocity for 500 and 2500 RPM are 0.952 and 0.981. This indicates that the degree of tangential slippage is 4.8% for a disk speed of 500 RPM and 1.9% for a disk speed of 2500 RPM. Higher disk speeds are desired for applications where atomization is desired. For practical applications such as the atomization of fuel in a combustion chamber is highly desired for efficient burning of fuel. In other applications,

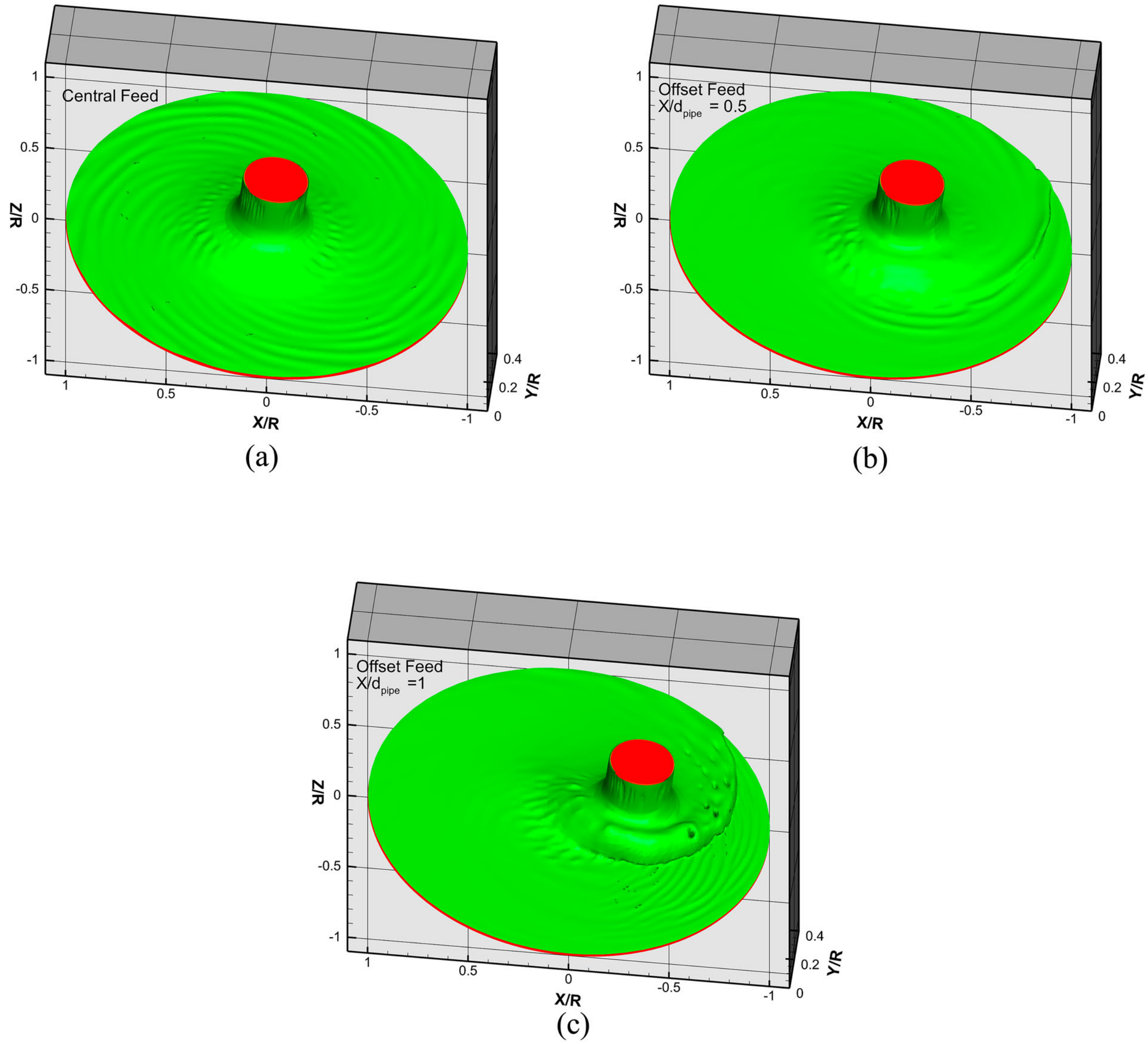

Figure 14. Instantaneous iso-surface of volume fraction 0.5 at $t/T_{\mathrm{rev}} = 5$ for the feed arrangements investigated.

such as pollutant dispersion or atomization of lubricating oil, this is not desired. Otherwise, it would be difficult to confine the fine particles.

Three distinct zones are identified based on mean radial film velocity as described by Burns et al. (2003). These zones are classified as: (i) the injection zone, in which liquid is slowed down because of viscous drag; (ii) the acceleration zone, in which liquid is accelerated because of the disk's centrifugal force and attains its maximum radial velocity; (iii) the synchronized zone, in which liquid expands over a large disk area and consequently the radial velocity drops down. However, the occurrence of these zones and their radial position is dependent on the operating and design parameters and on the fluid properties. The variation of the mean radial film velocity distribution with disk speed is shown in Figure 15(b). The three zones described above are identified and marked in Figure 15(b) based on the variation of the mean radial velocity. It can be observed that, irrespective of the disk speed, the basic flow features remain the same. All three zones are identified for the investigated flow conditions. However, the magnitude of the non-dimensional mean radial velocity decreases with an increase in disk speed.

3.2.2. Influence of liquid feed rate

The variation of the non-dimensional mean tangential and radial velocity with the liquid feed rate is shown in Figure 16 for the central feed arrangement at 1500 RPM. A significant impact of the liquid feed rate on the non-dimensional mean tangential velocity is observed as shown in Figure 16(a). The non-dimensional tangential velocity decreases with the increase in the flow rate. This is because of the increased viscous effect at a higher

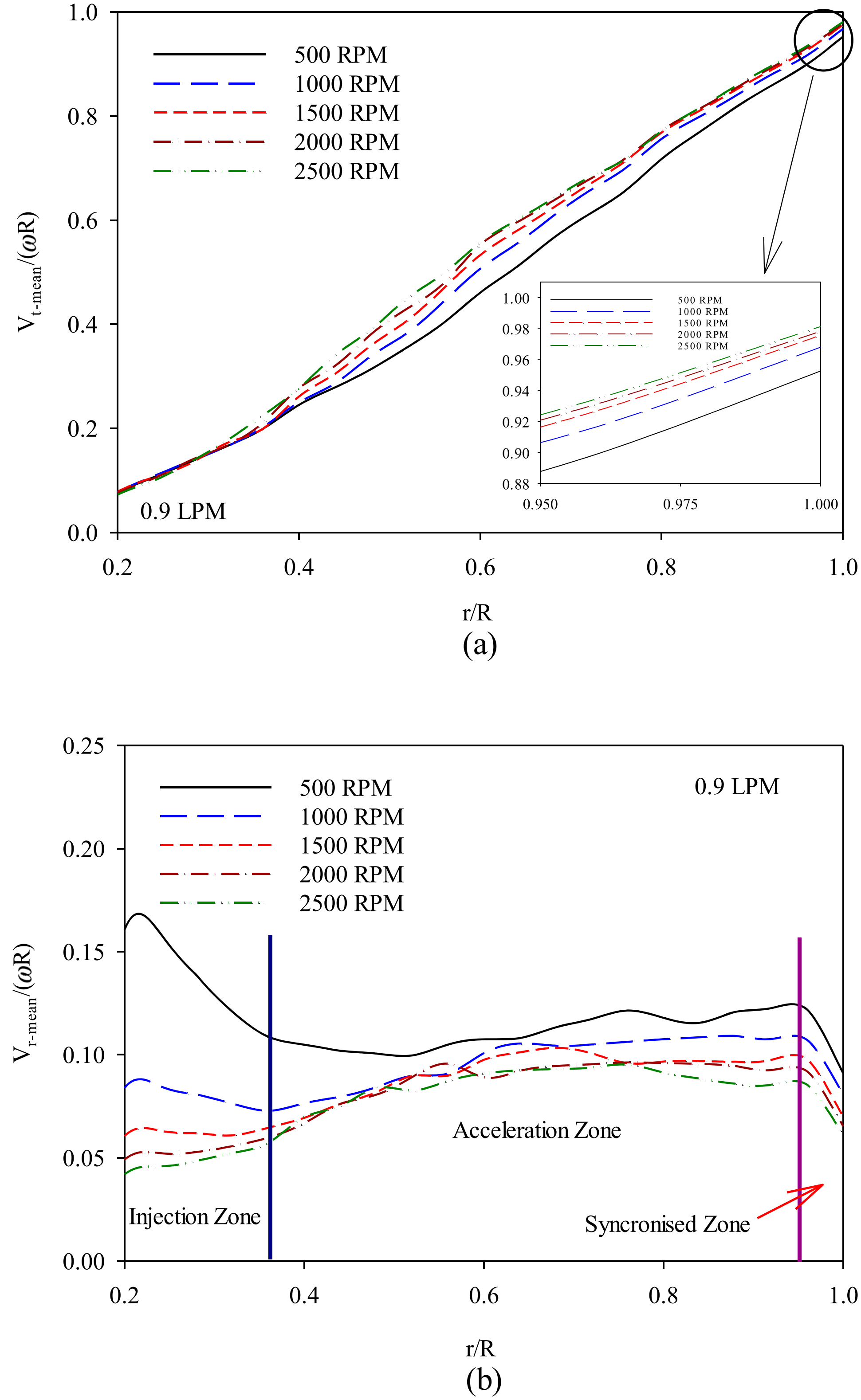

Figure 15. Non-dimensional mean film velocity variation with liquid feed rate: (a) tangential velocity; and (b) radial velocity.

flow rate for a fixed disk speed. The tangential slippage increases from 1.2% at 0.3 LPM to 8.8% at 2.4 LPM.

The variation of the non-dimensional mean radial velocity also indicates a profound impact of the liquid feed rate, as depicted in Figure 16(b). For the lowest investigated flow rate, 0.3 LPM, inertial effects are negligible. The liquid film accelerates from $0.2 \leq r/R \leq 0.38$ and attains a maximum mean radial velocity that remains

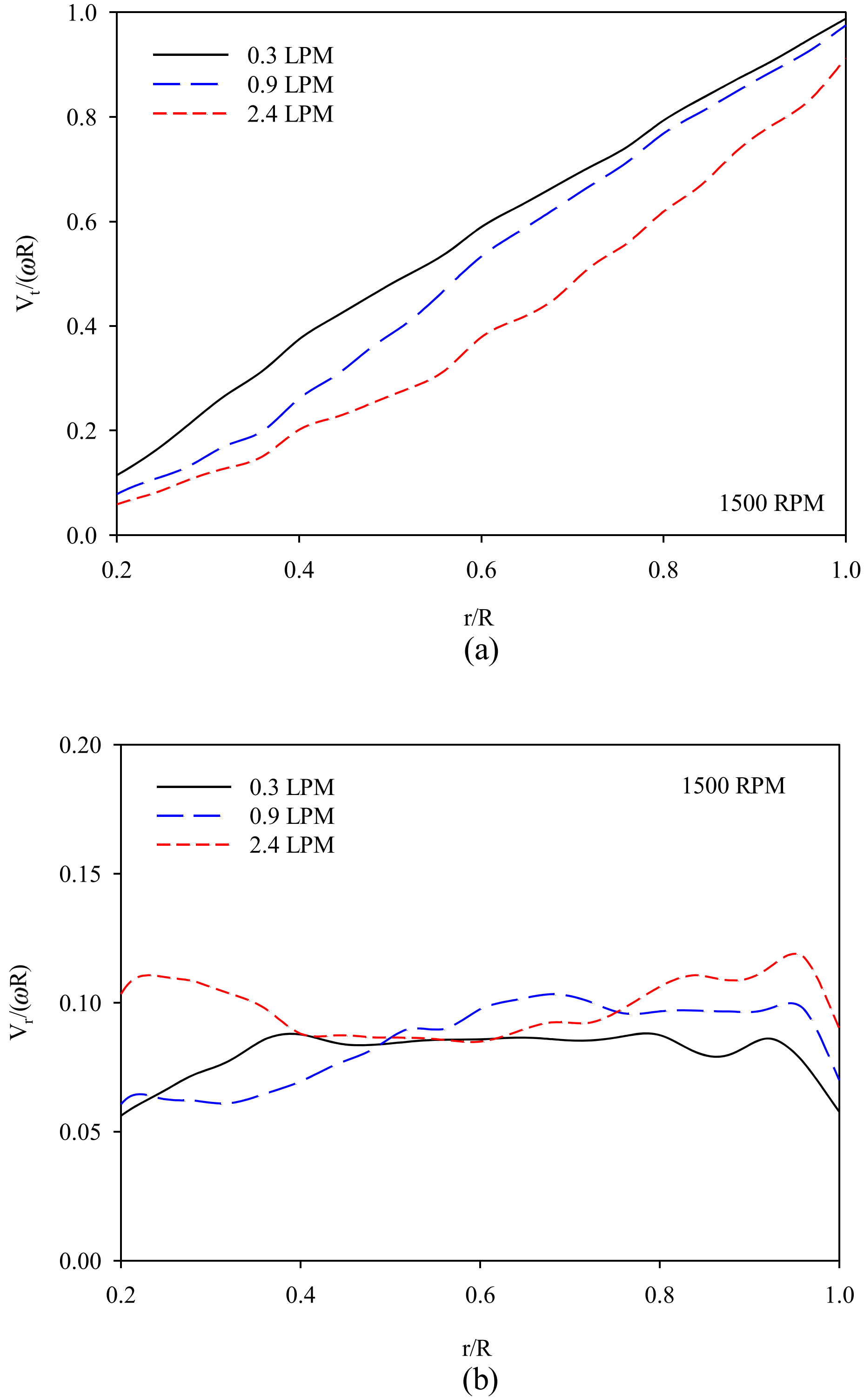

Figure 16. Non-dimensional mean film velocity variation with liquid feed rate: (a) tangential; and (b) radial.

almost constant until $r/R = 0.78$. Further expansion of the liquid results in the synchronization zone, leading to a drop in mean radial film velocity. On the contrary, inertial effects are significant for the 2.4 LPM case. The injection zone expands to $r/R = 0.4$; thereafter, the liquid film accelerates to $r/R = 0.96$ before moving to the synchronization zone.

3.2.3. Influence of offset feeding

The variation of non-dimensional mean tangential and radial velocity with the liquid feed rate is shown in Figure 17 for the central feed and offset feed arrangements at 1500 RPM and 0.9 LPM. The variation in the non-dimensional mean tangential film velocity towards the center of the disk ($0.2 \leq r/R \leq 0.5$) is due to the

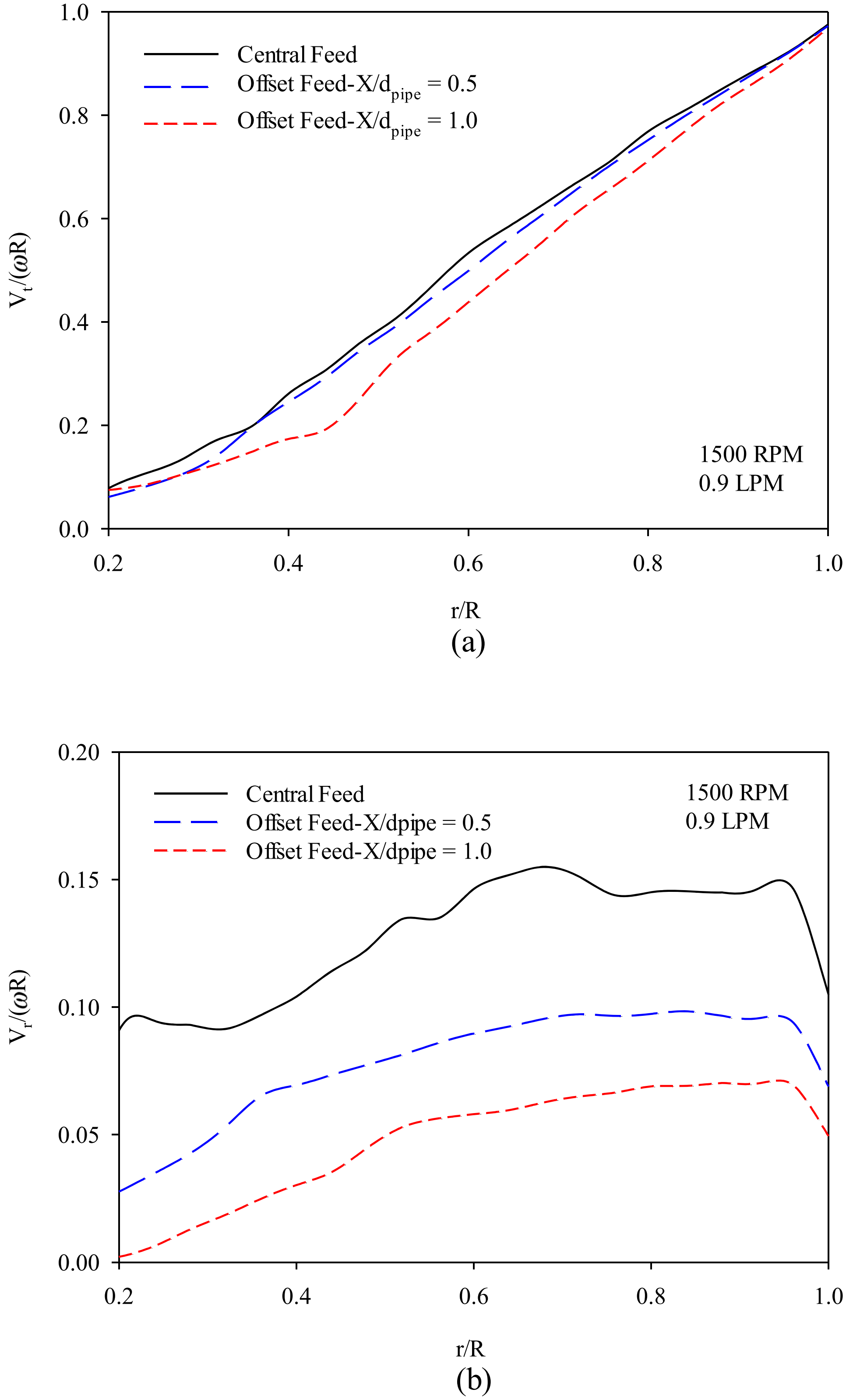

Figure 17. Non-dimensional mean film velocity variation with offset feed arrangement: (a) tangential; and (b) radial.

liquid feed arrangement. The mean film tangential velocity is almost identical for the investigated liquid feed configurations towards the edge of the disk. This indicates that the tangential slippage is not adversely affected by the offset feeding of the liquid. However, the mean radial film velocity for these liquid feed arrangements exhibits a significant difference, as shown in Figure 17(b). For the central feed arrangement, a drop in mean radial film velocity from $r/R = 0.2$ to 0.32 indicates the influence of inertial forces. Whereas, for the offset feed arrangements, liquid continues to accelerate from $r/R = 0.2$ to 0.95 and thus has a wider acceleration zone. The synchronization zone is almost identical for the liquid feed arrangements investigated.

3.3. Ligament formation and disintegration into droplets

Understanding the mechanism of liquid film disintegration can help in the efficient collection of lubricating oil in aeroengines. In the present study, two commonly observed disintegration regimes are targeted.

Ligament formation on a rotating disk is a transient phenomenon. In this study, the disintegration of free surface film flow into the ligament regime is presented using CD2 for a disk speed of 1500 RPM and liquid feed centrally at 0.9 LPM. Film thickness and film velocity components at the periphery of the disk (2 mm away from the edge) are extracted from CD1 to specify boundary conditions in CD2. The wave formations observed in the central part of the disk in CD1 become settled near the periphery, and a uniform mean film thickness is observed. The inlet conditions in CD2 are defined on the basis of this mean film thickness. The chronology of ligament formation is illustrated in Figure 18 in terms of non-dimensional time. For all the results presented in this section, the reference time (t) is measured from the beginning of the disk revolution in the second computational domain (CD2). The continuous film on the disk extends in the radial direction beyond the rim of the disk because of the centrifugal and inertial forces. At the lip of the disk, the surrounding air interacts with the film and makes it unstable. An annular ring is observed at $t/T_{\text{rev}} = 0.52$. Owing to the growth of instabilities at the liquid–air interface, this annular ring separates from the continuous film at $t/T_{\text{rev}} = 0.67$. After the separation of the ring, a torus structure is formed at $t/T_{\text{rev}} = 0.76$ because of the formation of waves due to surface tension and centrifugal forces. This torus structure keeps on extending in the radial direction until $t/T_{\text{rev}} = 0.81$. This is the inception of ligament formation.

The ligament spacing is determined by the torus structure, which is formed because of the interaction of air with the liquid. The Rayleigh–Taylor (RT) instability is mainly responsible for increasing perturbations at the air–liquid interface. The RT instability occurs owing to the destabilizing effect of the centrifugal force on the radial flow (Coquart et al., 2005). The liquid remains attached in the form of ligaments with the disk owing to the RT instability. Although the liquid is discharged by ligaments, the location of ligament formation is determined by the torus structure as shown in Figure 18(b). The spacing (λ_{RT}) between two consecutive torus structures is non-uniform because of the interaction with the air as marked by $\lambda_{\text{RT}-\text{L}}$ and $\lambda_{\text{RT}-\text{H}}$ in Figure 18(b). Here, subscripts L and H represent the minimum and maximum spacing between the torus structures. The average spacing between ligaments is found to be 2.8 mm for a disk speed of 1500 RPM.

The stretching and thinning of the ligaments continues to a critical length known as the 'Pinch Off' length, as can be seen in Figure 18(c) at $t/T_{\text{rev}} = 1.1$. Because of the absorption of liquid from the upstream, a bulbous shape is formed at the head of the ligament. After $t/T_{\text{rev}} = 1.1$, ligaments are extended to such an extent that surface tension dominates over viscous effects. Consequently, droplets are formed from the head of the ligaments. These droplets are called 'head droplets'. The size of these droplets is almost 10 times larger than the subsequent droplets and even larger than the diameter of the ligament itself. With the separation of head droplets, capillary waves are generated at the tip of the ligaments. These waves grow rapidly and propagate along the ligament. These waves are responsible for generating small spherical droplets.

3.4. Sheet formation and disintegration into droplets

Ligament-to-sheet transition occurs when the liquid flow rate is increased to a specific speed. In the present study, liquid sheet formation is investigated at a disk speed of 1500 RPM. The liquid feed rate is increased from 0.9 to 2.4 LPM, i.e. from the ligament formation regime to the sheet regime. In the sheet regime, liquid extends beyond the periphery of the disk. The radial extent of the liquid sheet is controlled by the centrifugal and surface tension forces. The hydrodynamic instabilities in the liquid film are amplified by the interaction of the liquid with the surrounding air, which eventually leads to further breakup of the sheet into ligaments or droplets.

The chronology of liquid sheet disintegration is illustrated in Figure 19 in terms of non-dimensional time for a disk speed of 1500 RPM and a liquid feed rate of 2.4 LPM. For all the results presented in this section, the reference time (t) is measured from the beginning of the disk revolution in the second computational domain. The continuous film on the disk extends in the radial direction beyond the rim of the disk because of the centrifugal and inertial forces. Consequently, a liquid sheet is formed at $t/T_{\text{rev}} = 0.167$, as depicted in Figure 19. This sheet remains suspended in the surrounding air. The surface tension force acts to minimize the radial expansion of the suspended sheet. Because of this, a thicker liquid film

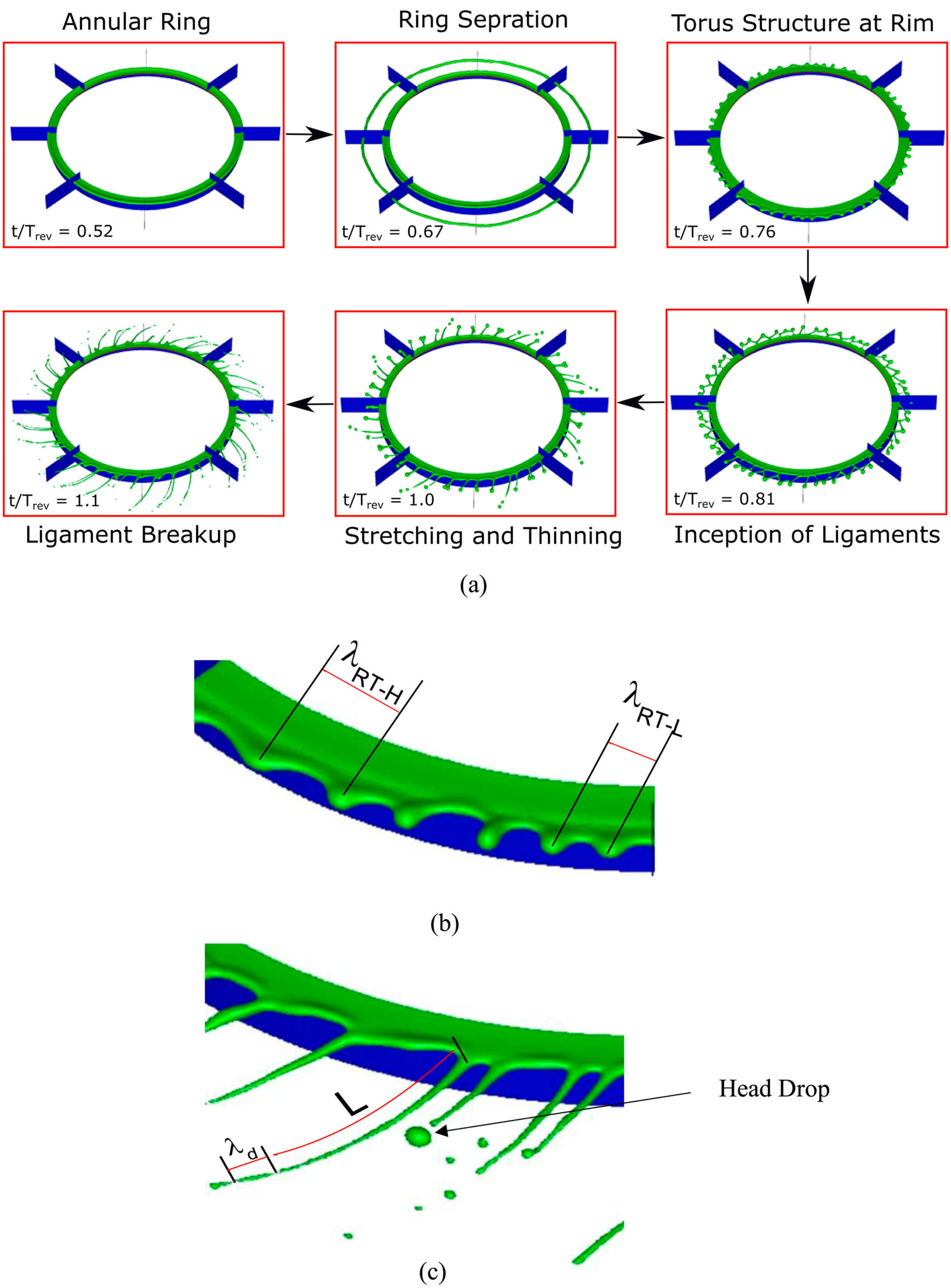

Figure 18. (a) Chronology of ligament formation on a rotating disk. Magnified zoomed views of disk rim at: (b) $t/T_{rev} = 0.76$; and (c) $t/T_{rev} = 1.1$.

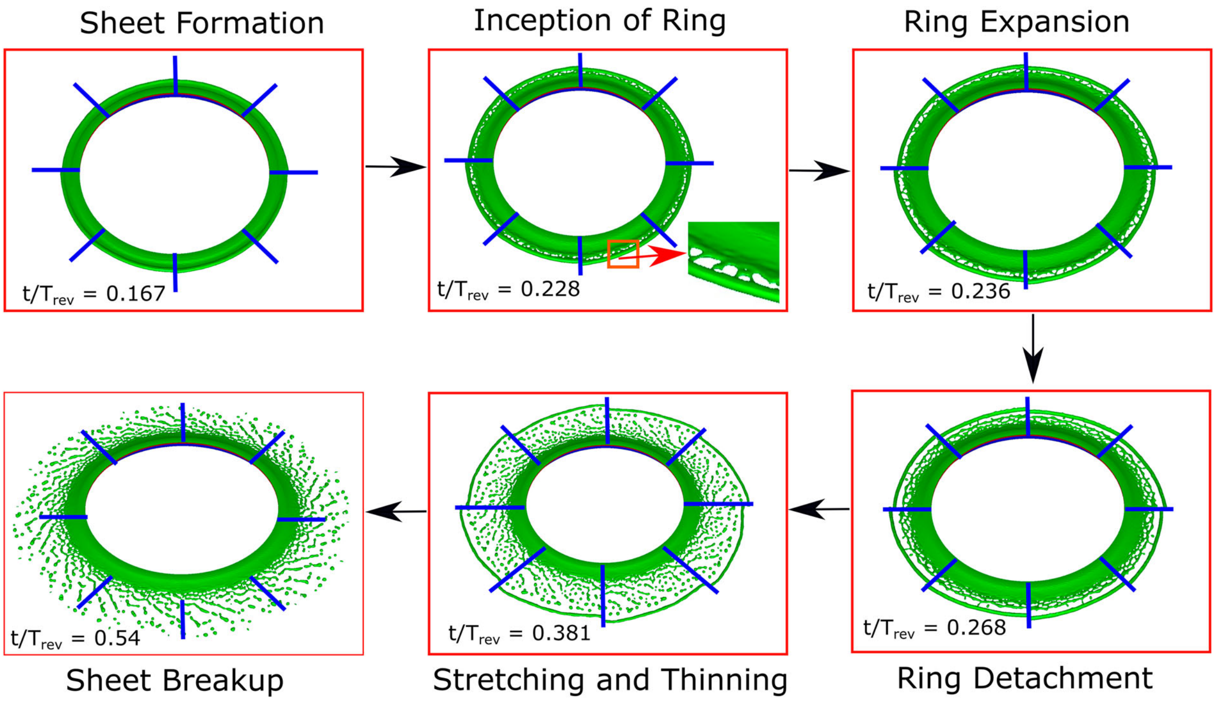

Figure 19. Chronology of sheet formation and breakup on a rotating disk.

on the outer edge of the suspended sheet is observed. The surface tension force on a continuous expanding liquid film results in the formation of an annular ring as observed at $t/T_{\text{rev}} = 0.228$. The outer edge of this ring is relatively thicker as compared to the end towards the lip of the disk. The film thickness keeps on decreasing as the liquid moves in the radial direction. When the surface tension force overcomes the centrifugal and inertial forces, ligaments appear in between the annular ring and the continuous sheet. These ligaments act as a bridge between the annular ring and the continuous film and keep on feeding the annular ring as it moves in the radial direction, as observed at $t/T_{\text{rev}} = 0.236$. Owing to the growth of instabilities at the liquid–air interface and thinning of the ligaments, this annular ring separates from the continuous film at $t/T_{\text{rev}} = 0.268$. It should be noted that the formation of the annular ring and its separation from the continuous film is quicker in the sheet regime as compared to the ligament regime. The reason for this behavior is the higher flow rate of liquid in the sheet regime as compared to the ligament regime. Film momentum and the magnitude of the centrifugal and inertial forces increase because of the increased mass flow rate.

At the edges of the disk, the aerodynamic forces exerted by the surrounding air exceed the interfacial tension. Consequently, unstable waves are formed. These waves keep on amplifying as the liquid sheet extends in the radial direction. Stretching of the suspended sheet followed by thinning is observed at $t/T_{\text{rev}} = 0.381$ before the continuous breakup of the liquid sheet at $t/T_{\text{rev}} = 0.54$. For the operating parameters investigated in the present study, a combined rim and wave disintegration mechanism is observed. Fraser et al. (1963) proposed a correlation for estimating the radial extent of the sheet on a rotating cup for the combined rim and wave disintegration mechanism. This correlation is given in Equation (9):

$$a_{rw} = \left[15.6 \times 10^4 \nu_r^{0.185} \frac{(\sigma Q_m)^{2/3}}{(N d_L)^2} + \frac{{d_L}^2}{4} \right]^{1/2} - \frac{d_L}{2} \tag{9}$$

where ν_r is the ratio of the kinematic viscosities of oil and water, σ is surface tension, Q_m is liquid mass flow rate, N is cup speed and d_L is cup diameter at the lip.

The radial extent of the sheet estimated from the correlation proposed by Fraser et al. (1963) is 3.15 mm for the operating conditions of the present study. The numerically obtained radial extent of the sheet in the present study is around 3.05 mm, which is in excellent agreement with the correlation proposed by Fraser et al. (1963).

4. Conclusions and future work

In the present study, a numerical methodology is developed to investigate free surface film flow and its subsequent disintegration mechanism on a rotating disk for incompressible and isothermal conditions. The presented CFD model and methodology is of the very first kind where both film formation on a rotating disk and liquid film disintegration into ligaments and the sheet regime are successfully investigated using the volume of fluid method. The presented computational methodology can easily be reproduced and can act as a benchmark for modeling liquid film formation as well as the liquid disintegration phenomenon. Typically, the presence of surface waves is ignored in most analytical and numerical studies, despite experimental evidence for these waves. In the present study, the formation and breakup of surface waves and their qualitative comparison with experimental studies are discussed. The following presents the main conclusions from this study.

- The film thickness profile on the disk resembles the formation of spiral waves at 500 RPM and an irregular breakup of the spiral waves for a disk speed of 1000 RPM. At higher speeds, a smooth and thin liquid film is observed on the disk.
- Offset feeding of the liquid onto the disk alters the wave formation and breakup of the spiral waves. The formation of spiral waves that unwind in the direction of rotation is observed in the case of the central feed arrangement. These waves cover the entire disk but, in the case of the offset feed arrangement, waves occur only on a segment of the disk ($0 \leq \theta \leq \pi$).
- At the edge of the disk, the non-dimensional mean film velocity increases with an increase in the rotational speed. Consequently, the degree of tangential slippage decreases from 4.8% at 500 RPM to 1.9% at 2500 RPM. Three distinct zones of the film flow on the rotating disk are identified, based on mean radial film velocity. These zones are classified as (i) the injection zone, (ii) the acceleration zone and (iii) the synchronized zone.
- Liquid film disintegration mechanisms, which are rather complex phenomena, are accurately captured by the present numerical model. Liquid sheet breakup analysis indicates that ligaments are formed at the lip of the disk owing to Rayleigh–Taylor instability, whereas liquid sheet breakup is due to combined rim and wave disintegration for the parameters investigated in this study.

In the present study, the disintegration of liquid is modeled only for the central feed arrangement. Oblique and offset feed arrangements are used to feed lubricating oil in aeroengine components. Hence, future work will involve:

- the modeling of disintegration mechanisms for oblique and offset feed arrangements;
- quantification of droplet distribution from the various feed arrangements;
- modeling of heat transfer and quantifying the impact of liquid film evaporation on free surface film flows and subsequent disintegration.

Acknowledgements

The authors are thankful to Rolls Royce plc and the University of Nottingham for providing the High Performance Computing Facility.

Disclosure statement

No potential conflict of interest was reported by the authors.

Funding

This work was supported by funding from the Clean Sky 2 and European Union's Horizon 2020 research and innovation program, the Horizon 2020 Framework Programme [Grant Agreement No. 724625]; Athena at HPC Midlands+, funded by the EPSRC [Grant EP/P020232/1].

References

ANSYS Inc. (US). (2020). ANSYS Fluent theory guide, release2020R1. In ANSYS Fluent theory guide.

Appelquist, E., Schlatter, P., Alfredsson, P. H., & Lingwood, R. J. (2018). Turbulence in the rotating-disk boundary layer investigated through direct numerical simulations. *European Journal of Mechanics, B/Fluids*, *70*, 6–18. https://doi.org/10.1016/j.euromechflu.2018.01.008

Bhatelia, T. J., Utikar, R. P., Pareek, V. K., & Tade, M. O. (2009, December 9–11). Characterizing liquid film thickness in spinning disc reactors. In *Proceedings of the Seventh International Conference on CFD in the Minerals and Process Industries*, CSIRO, Melbourne, Australia.

Bizjan, B., Širok, B., Hočevar, M., & Orbanić, A. (2014). Liquid ligament formation dynamics on a spinning wheel. *Chemical Engineering Science*, *119*, 187–198. https://doi.org/10.1016/j.ces.2014.08.031

Brackbill, J. U., Kothe, D. B., & Zemach, C. (1992). A continuum method for modeling surface tension. *Journal of Computational Physics*, *100*(2), 335–354. https://doi.org/10.1016/0021-9991(92)90240-Y

Brauer, H. (1958). Stoffaustausch beim rieselfilm. *Chemie Ingenieur Technik*, *30*(2), 75–84. https://doi.org/10.1002/cite.330300205

Bristot, A., Morvan, H. P., & Simmons, K. A. (2016, June 13–17). Evaluation of a volume of fluid CFD methodology for the oil film thickness estimation in an aero-engine bearing chamber. In *Proceedings of ASME Turbo Expo 2016: Turbomachinery Technical Conference and Exposition*, Seoul, South Korea (pp. 1–11).

Burns, J. R., Ramshaw, C., & Jachuck, R. J. (2003). Measurement of liquid film thickness and the determination of spin-up radius on a rotating disc using an electrical resistance technique. *Chemical Engineering Science*, *58*(11), 2245–2253. https://doi.org/10.1016/S0009-2509(03)00091-5

Cageao, P. P., Johnson, K., Ambrose, S., & Omar, R. (2022, June 13–17). GT2022-82195 experimental investigation into oil shedding from a rotating cup geometry. In *Proceedings of ASME Turbo Expo 2022: Turbomachinery Technical Con-*

ference and Exposition GT2022, Rotterdam, Netherlands, GT2022-82195, 1–14. https://nottingham-repository.worktribe.com/output/7733321

Charwat, A. F., Kelly, R. E., & Gazley, C. (1972). The flow and stability of thin liquid films on a rotating disk. *Journal of Fluid Mechanics*, *53*(2), 227–255. https://doi.org/10.1017/S0022112072000138

Coquart, L., Sipp, D., & Jacquin, L. (2005). Mixing induced by Rayleigh-Taylor instability in a vortex. *Physics of Fluids*, *17*(2), 1–4. https://doi.org/10.1063/1.1852580

Egorov, Y. (2004). Validation of CFD codes with PTS-relevant test cases EVOLECORA-D07.

Espig, H., & Hoyle, R. (1965). Waves in a thin liquid layer on a rotating disk. *Journal of Fluid Mechanics*, *22*(4), 671–677. https://doi.org/10.1017/S0022112065001052

Fraser, R. P., Dombrowski, N., & Routley, J. H. (1963). The filming of liquids by spinning cups. *Chemical Engineering Science*, *18*(6), 323–337. https://doi.org/10.1016/0009-2509(63)80026-3

Frost, A. R. (1981). Rotary atomization in the ligament formation mode. *Journal of Agricultural Engineering Research*, *26*(1), 63–78. https://doi.org/10.1016/0021-8634(81)90127-X

Gibbs Inteaz Alli, F., Mulligan, C. N., & Bernard, S. K. (1999). Encapsulation in the food industry: A review. *International Journal of Food Sciences and Nutrition*, *50*(3), 213–224. https://doi.org/10.1080/096374899101256

Glahn, A., Busam, S., Blair, M. F., Allard, K. L., & Wittig, S. (2002). Droplet generation by disintegration of oil films at the rim of a rotating disk. *Journal of Engineering for Gas Turbines and Power*, *124*(1), 117–124. https://doi.org/10.1115/1.1400753

Hinze, J. O., & Milborn, H. (1950). Atomization of liquids by means of a rotating cup. *Journal of Applied Mechanics*, *17*(2), 145–153. https://doi.org/10.1115/1.4010093

Imayama, S., Henrik Alfredsson, P., & Lingwood, R. J. (2013). An experimental study of edge effects on rotating-disk transition. *Journal of Fluid Mechanics*, *716*, 638–657. https://doi.org/10.1017/jfm.2012.564

Kheyfets, V. O., & Kieweg, S. L. (2013). Experimental and numerical models of three-dimensional gravity-driven flow of shear-thinning polymer solutions used in vaginal delivery of microbicides. *Journal of Biomechanical Engineering*, *135*(6), 061009. https://doi.org/10.1115/1.4024140

Lee, J., Lee, H., Park, H., Cho, G. H., Kim, D., & Cho, J. (2021). Design optimization of a vane type pre-swirl nozzle. *Engineering Applications of Computational Fluid Mechanics*, *15*(1), 164–179. https://doi.org/10.1080/19942060.2020.1847199

Lepehin, G. I., & Riabchuk, G. V. (1975). Temperature distribution in film of viscous liquid with heating on a rotating disk. *Rheology in Processes and Apparatus of Chemical Technology*, *82*, 82–91.

Liu, G., Gong, W., Wu, H., & Lin, A. (2021). Experimental and CFD analysis on the pressure ratio and entropy increment in a cover-plate pre-swirl system of gas turbine engine. *Engineering Applications of Computational Fluid Mechanics*, *15*(1), 476–489. https://doi.org/10.1080/19942060.2021.1884600

Liu, J., Yu, Q., & Guo, Q. (2012). Experimental investigation of liquid disintegration by rotary cups. *Chemical Engineering Science*, *73*, 44–50. https://doi.org/10.1016/j.ces.2012.01.010

Mantripragada, V. T., & Sarkar, S. (2017). Prediction of drop size from liquid film thickness during rotary disc atomization process. *Chemical Engineering Science*, *158* (June 2016), 227–233. https://doi.org/10.1016/j.ces.2016.10.027

Nicoli, A., Singh, K., Jefferson-loveday, R., Ambrose, S., & Mouvanal, S. (2022, June 13–17). Numerical simulation of multi-scale oil film on a rotating cup using VOF and coupled Eulerian thin-film-DPM approaches. In *Proceedings of ASME Turbo Expo 2022: Turbomachinery Technical Conference and Exposition GT2022*, Rotterdam, Netherlands, GT2022-82533, 1–13.

Pan, Y., Witt, P. J., & Xie, D. (2010). CFD simulation of free surface flow and heat transfer of liquid slag on a spinning disc for a novel dry slag granulation process. *Progress in Computational Fluid Dynamics, An International Journal*, *10*(5/6), 292. https://doi.org/10.1504/pcfd.2010.035362

Rauscher, J. W., Kelly, R. E., & Cole, J. D. (1973). An asymptotic solution for the laminar flow of a thin film on a rotating disk. *Journal of Applied Mechanics*, *40*(1), 43–47. https://doi.org/10.1115/1.3422970

Rice, J., Faghri, A., & Cetegen, B. (2005). Analysis of a free surface film from a controlled liquid impinging jet over a rotating disk including conjugate effects, with and without evaporation. *International Journal of Heat and Mass Transfer*, *48*(25–26), 5192–5204. https://doi.org/10.1016/j.ijheatmasstransfer.2005.07.022

Sun, H., Chen, G., Wang, L., & Wang, F. (2015). Ligament and droplet generation by oil film on a rotating disk. *International Journal of Aerospace Engineering*, *2015*, 1–14. https://doi.org/10.1155/2015/769862

Turkyilmazoglu, M. (2019). Direct contact melting due to a permeable rotating disk. *Physics of Fluids*, *31*(2), 023603. https://doi.org/10.1063/1.5086724

Turkyilmazoglu, M. (2022). Flow and heat over a rotating disk subject to a uniform horizontal magnetic field. *Zeitschrift Fur Naturforschung – Section A Journal of Physical Sciences*, *77*(4), 329–337. https://doi.org/10.1515/zna-2021-0350

Wang, D., Jin, H., Ling, X., Peng, H., Yu, J., & Cui, Z. (2020). Regulation of velocity zoning behaviour and hydraulic jump of impinging jet flow on a spinning disk reactor. *Chemical Engineering Journal*, *390*(1800), 124392. https://doi.org/10.1016/j.cej.2020.124392

Wang, D., Ling, X., & Peng, H. (2014). Theoretical analysis of free-surface film flow on the rotary granulating disk in waste heat recovery process of molten slag. *Applied Thermal Engineering*, *63*(1), 387–395. https://doi.org/10.1016/j.applthermaleng.2013.11.033

Wang, D., Ling, X., & Peng, H. (2015). Simulation of ligament mode breakup of molten slag by spinning disk in the dry granulation process. *Applied Thermal Engineering*, *84*, 437–447. https://doi.org/10.1016/j.applthermaleng.2015.03.003

Wang, D., Ling, X., Peng, H., Cui, Z., & Yang, X. (2016). Experimental investigation of ligament formation dynamics of thin viscous liquid film at spinning disk edge. *Industrial & Engineering Chemistry Research*, *55*(34), 9267–9275. https://doi.org/10.1021/acs.iecr.6b01428

Woods, W. P. (1995). *The hydrodynamics of thin liquid films flowing over a rotating disc*. University of Newcastle.

Wu, J. J., Wang, H., Zhu, X., Liao, Q., & Ding, B. (2015). Centrifugal granulation performance of liquid with various viscosities for heat recovery of blast furnace slag. *Applied Thermal Engineering*, *89*, 494–504. https://doi.org/10.1016/j.applthermaleng.2015.06.031

Yuan, H., Peng, H., He, X., Chen, L., & Zhou, J. (2021). Double droplet splashing on a thin liquid film with a pseudopotential lattice Boltzmann method. *Engineering Applications of Computational Fluid Mechanics*, *15*(1), 964–984. https://doi.org/10.1080/19942060.2021.1934547